Check for updates

Geochemistry, Geophysics, Geosystems®

AGU ADVANCING EARTH AND SPACE SCIENCE

RESEARCH ARTICLE
10.1029/2022GC010387

Contrasting Volcanic Deformation in Arc and Ocean Island Settings Due To Exsolution of Magmatic Water

Stanley Tze Hou Yip[1,2], Juliet Biggs[1,2], Marie Edmonds[1,3], Philippa Liggins[3], and Oliver Shorttle[3]

[1]Centre for the Observation and Modelling of Earthquakes, Volcanoes and Tectonics (COMET), [2]School of Earth Sciences, University of Bristol, Bristol, UK, [3]Department of Earth Sciences, University of Cambridge, Cambridge, UK

Key Points:

- We use petrological data and a thermodynamic framework to model volcanic deformation and SO_2 degassing
- We compiled observations from 94 basaltic eruptions and did a systematic study of parameter space including H_2O content
- High magmatic volatile content contributes to the lack of deformation observed during arc basalt eruptions

Supporting Information:

Supporting Information may be found in the online version of this article.

Correspondence to:

S. T. H. Yip,
stanley.th.yip@bristol.ac.uk

Citation:

Yip, S. T. H., Biggs, J., Edmonds, M., Liggins, P., & Shorttle, O. (2022). Contrasting volcanic deformation in arc and ocean island settings due to exsolution of magmatic water. *Geochemistry, Geophysics, Geosystems*, *23*, e2022GC010387. https://doi.org/10.1029/2022GC010387

Received 25 FEB 2022
Accepted 7 JUN 2022

Author Contributions:

Conceptualization: Stanley Tze Hou Yip, Juliet Biggs, Marie Edmonds
Data curation: Stanley Tze Hou Yip
Formal analysis: Stanley Tze Hou Yip
Funding acquisition: Juliet Biggs
Investigation: Stanley Tze Hou Yip
Methodology: Stanley Tze Hou Yip, Juliet Biggs, Marie Edmonds
Resources: Stanley Tze Hou Yip, Juliet Biggs, Marie Edmonds
Software: Stanley Tze Hou Yip, Philippa Liggins
Supervision: Juliet Biggs, Marie Edmonds

© 2022. The Authors.
This is an open access article under the terms of the Creative Commons Attribution License, which permits use, distribution and reproduction in any medium, provided the original work is properly cited.

Abstract Two of the most widely observed co-eruptive volcanic phenomena—Ground deformation and volcanic outgassing—Are fundamentally linked via the mechanism of magma degassing and the development of compressibility, which controls how the volume of magma changes in response to a change in pressure. Here we use thermodynamic models—Constrained by petrological data—To reconstruct volatile exsolution and the consequent changes in magma properties. We use the fraction of SO_2 exsolved during decompression to predict co-eruptive SO_2 flux and magma compressibility to predict co-eruptive surface deformation (both normalized by erupted volume). We conduct sensitivity tests using properties of typical basalts to assess how varying magma volatile content, crustal properties, and chamber geometry affect co-eruptive deformation and degassing. We find that magmatic H_2O content has the most impact on both SO_2 flux and volume change. Our findings have general implications for typical basaltic systems in arc and ocean island settings. The higher water content of arc magmas makes them more compressible than ocean island magmas and leads to muted or non-existent deformation being observed during arc eruptions. Our models are consistent with observation: Deformation has been detected during 48% of basaltic eruptions in ocean island settings (16/33) during the satellite era (2005–2020), but only 11% of basaltic eruptions in arc settings (7/61).

Plain Language Summary Volcano monitoring provides a wealth of data upon which to base activity forecasts, yet we lack quantitative models to integrate two of the most widely observed eruptive parameters: Ground deformation and volcanic gas fluxes. When magma exsolves volatiles (water, carbon dioxide, sulfur) during storage in the crust prior to eruptions, the fluid bubbles cause the magma to become compressible, and behave like a sponge. The effect of this degassing is that when pressure changes in the magma chamber (due to eruption, or due to recharge), the gas bubbles expand or contract in response, effectively maintaining a near-constant volume for the magma. Understanding the effect of magmatic gas on volume changes is key to developing integrated, satellite-based volcano monitoring approaches.

1. Introduction

The increasing number of satellite missions launched in the past decade has driven an explosion in data for studying the Earth's dynamic processes (Biggs & Wright, 2020; Carn et al., 2017; Chaussard et al., 2013; Furtney et al., 2018; Morales Rivera et al., 2016). The array of sensors onboard satellites routinely provide near real-time observations of volcanic eruptions such as SO_2 plumes and clouds (e.g., Carboni et al., 2016; Carn et al., 2016; Ge et al., 2016) and ground deformation (e.g., Biggs & Pritchard, 2017; Ebmeier et al., 2018; Pritchard et al., 2018), both of which are key indicators of eruption progress and may be used to track eruptive activity and understand pre-eruptive magma storage conditions. However, observations reveal that not all volcanoes exhibit pre- or co-eruptive deformation (Biggs, Ebmeier, et al., 2014; Reath et al., 2020; Rivalta & Segall, 2008); the causes of the wide variation in deformation systematics between volcanoes and between tectonic settings are not well understood (Chaussard & Amelung, 2014; Ebmeier et al., 2013a; Piochi et al., 2005).

Reconciling observations of volcanic deformation and degassing can help identify the conditions that lead to the lack of observations of ground deformation (Kilbride et al., 2016; Reath et al., 2020). The magmatic processes that drive volcanic deformation and degassing are fundamentally linked: Exsolution of volatiles from silicate melt in crustal magma reservoirs (during isobaric cooling and crystallisation, also termed as “second boiling”, or due to decompression) causes magma to become compressible, thereby allowing it to change its volume in response to pressure perturbations experienced by the magma during eruption and recharge (Kilbride et al., 2016;

15252027, 2022, 7, Downloaded from https://agupubs.onlinelibrary.wiley.com/doi/10.1029/2022GC010387 by Alaska State Library, Wiley Online Library on [23/06/2025]. See the Terms and Conditions (https://onlinelibrary.wiley.com/terms-and-conditions) on Wiley Online Library for rules of use; OA articles are governed by the applicable Creative Commons License

Validation: Stanley Tze Hou Yip, Juliet Biggs, Marie Edmonds, Philippa Liggins, Oliver Shorttle
Visualization: Stanley Tze Hou Yip
Writing – original draft: Stanley Tze Hou Yip
Writing – review & editing: Stanley Tze Hou Yip, Juliet Biggs, Marie Edmonds, Oliver Shorttle

Wong et al., 2017; Wong & Segall, 2020; Woods & Huppert, 2003). While it is becoming increasingly common to compile multisensor data (e.g., Furtney et al., 2018; Reath et al., 2019, 2020), until recently there has not been a quantitative framework to jointly interpret observations of volcanic deformation and degassing, including CO_2 and SO_2 gas fluxes (Girona et al., 2014; Kilbride et al., 2016; Wong & Segall, 2020).

Thermodynamic models, constrained by petrological data, may be used to calculate the varying proportions of melt, crystals and exsolved volatiles in shallow magmatic reservoirs under a range of pressure, temperature and magma composition conditions (e.g., Burgisser et al., 2015; Gualda et al., 2012; Liggins et al., 2020, 2021; Papale et al., 2006). The total volume of gas emitted during an eruption is a combination of gas stored in the chamber (generated by decompression prior to reaching the chamber and second boiling), and additional gas exsolved during decompression and ascent from the chamber to the surface. For explosive intermediate and silicic eruptions, it has been proposed that much of the sulfur outgassed is derived from a pre-existing exsolved volatile phase (Wallace, 2001, 2005). For effusive eruptions however, where magma ascends more slowly to the surface, the outgassed sulfur is derived from both second boiling and shallow decompressional degassing. Since the physicochemical properties of magmas are interdependent, magma properties such as density and compressibility can be calculated using the law of conservation of mass (Huppert & Woods, 2002; Spera, 2000). The compressibility of magma and the properties of the chamber, including geometry and host rheology, control the co-eruptive volume change, which consequently affects co-eruptive ground deformation at the surface (Dieterich & Decker, 1975; Edmonds et al., 2019; Head et al., 2019; Huppert & Woods, 2002; Sigmundsson et al., 2020; Zhan & Gregg, 2019).

Previous work by Kilbride et al. (2016) introduced a thermodynamic framework for reconciling satellite observations of atmospheric sulfur yield and volcanic deformation during discrete explosive eruptions (where there is assumed to be little volatile exsolution during magma ascent; i.e., all of the outgassed sulfur is derived from a pre-existing volatile phase; (Wallace, 2003)). The framework uses thermodynamic models to illustrate the effect of initial magmatic volatile content (H_2O, CO_2) and oxygen fugacity on SO_2 degassing and volcanic deformation. Sensitivity analyses were performed for magma of rhyolitic composition to provide model predictions of magma properties as a function of depth (Kilbride et al., 2016). Kilbride et al. (2016) then compared their model predictions to observations from 11 discrete explosive eruptions to illustrate the factors controlling volcanic deformation and degassing.

In this study, we use a thermodynamic framework to evaluate observations of volcanic deformation between eruptions of arc and ocean island basalts (which have more and less magmatic water respectively, see later for ranges). We extend the thermodynamic framework developed by Kilbride et al. (2016) to enable large-scale analyses, such as sensitivity tests and Monte-Carlo simulations, for basaltic eruptions (see Table 1). The sensitivity tests use properties typical for basaltic magmas (i.e., 45%–52% SiO_2) to explore how varying initial magmatic volatile contents (H_2O, CO_2, S) and oxygen fugacity affect magma properties such as density and compressibility, and consequently volcanic deformation and degassing. We also consider the effects of variable crustal shear modulus μ and chamber geometry on co-eruptive volcanic deformation. Finally, we compare the properties of basaltic magmas from arc and ocean island settings arising from their different volatile contents using Monte-Carlo simulations and discuss the implications for satellite observations of deformation during eruptions in different tectonic settings.

2. Background: Observations of Volcanic Deformation and Degassing

Satellites with short repeat time and high spatial resolution provide consistent spatio-temporal coverage for monitoring volcanoes on regional to global scales (e.g., TerraSAR-X, Sentinel-1), which is particularly valuable for monitoring volcanoes with few or no ground-based stations (e.g., Carboni et al., 2016; Coppola et al., 2020; Delgado et al., 2017; Ebmeier et al., 2016; Pritchard et al., 2018; Telling et al., 2015). Interferometric Synthetic Aperture Radar (InSAR) is a satellite technique that measures the phase change between pairs of satellite radar images to generate maps of surface displacement, which may be used to monitor volcanoes exhibiting deformation in response to changes in magma activity. However, while many volcanoes exhibit pre-eruptive inflation associated with magma intrusion and/or co-eruptive deflation during magma withdrawal, some do not (Biggs & Pritchard, 2017; Ebmeier et al., 2018; Moran et al., 2006; Rivalta & Segall, 2008). One possible cause of the lack of deformation is the presence of an exsolved gas phase in the magma at chamber depths that is more

15252027, 2022, 7, Downloaded from https://agupubs.onlinelibrary.wiley.com/doi/10.1029/2022GC010387 by Alaska State Library, Wiley Online Library on [23/06/2025]. See the Terms and Conditions (https://onlinelibrary.wiley.com/terms-and-conditions) on Wiley Online Library for rules of use; OA articles are governed by the applicable Creative Commons License

Table 1
Parameter Space Used for Sensivity Tests (Section 4) and Monte Carlo Simulations of Arc and Ocean Island Basalts (Section 5.1): Initial H_2O, CO_2 and S Contents, and Oxygen Fugacity (f_{O_2})

Parameters	H_2O (wt%)	CO_2 (ppm)	f_{O_2}	S (ppm)
Sensitivity test	2.0 (1.0–3.0)	3000 (1000–5000)	NNO (NNO − 1-NNO + 2)	2000 (1000–3000)
Arc basalts	3.9 ± 0.4	4000 ± 1000	3000 ± 1000	NNO + 1.4 ± 1
Ocean island basalts	1.0 ± 0.2	6500 ± 3500	1600 ± 1000	NNO + 0.7 ± 0.9

Note. The sensitivity tests vary the chosen parameter (bracketed) while holding all other parameters constant (unbracketed).

compressible than the surrounding crust and silicate melt (Huppert & Woods, 2002; Kilbride et al., 2016; Woods & Huppert, 2003).

The most volumetrically significant volcanic volatile species produced during an eruption are H_2O and CO_2, yet it is difficult to distinguish these volatiles from atmospheric background in satellite measurements. In contrast, volcanic SO_2 has a strong absorption signal in the near-ultraviolet and infrared spectrum, and thus can be measured using satellite-based spectrometers (e.g., Carboni et al., 2016; Carn et al., 2016). The total mass of SO_2 emitted from a volcano is the integrated sum of degassing in the chamber and during ascent of magma to the surface.

Conceptual models of magmatic systems may be used to understand different degassing configurations and their impact on monitoring signals (Figure 1). Volatiles including H_2O, CO_2 and SO_2, are more soluble at higher pressures and hence they are largely dissolved in silicate melt in deep magmatic systems (Figure 1a). Volatiles exsolve during magma decompression, but if magma stalls in a chamber and cools, volatiles also exsolve during isobaric cooling and crystallisation, a process termed "second boiling" (Candela & Piccoli, 1998).

For an explosive eruption, the high magma ascent rate limits volatile exsolution between the chamber and the surface (Figure 1b) and we make the simplifying assumption here that the gas emitted during the eruption is sourced entirely from the pre-eruptive exsolved volatile phase. In this case the amount of gases released (per unit of magma erupted) may be used to constrain the compressibility of the magma in the chamber prior to eruption, which will be related to the amount of deformation observed. In contrast, effusive eruptions involve a low magma ascent rate, such that volatiles exsolve extensively in the conduit (Figure 1c). In this case, the gases released during eruptions are mostly produced during magma ascent and cannot simply be related to the properties of the magma in the chamber prior to eruption without careful reconstruction of the degassing process using a thermodynamic model. Owing to the high diffusivity of volatiles in basaltic melts at high temperature, basaltic magma is likely to undergo extensive degassing during shallow magma ascent and eruption (e.g., Hurwitz & Anderson, 2019; Sigmarsson et al., 2013; Zhang & Stolper, 1991).

3. Methodology

3.1. Thermodynamic Modeling

Volatile solubility can be defined as the concentration of a volatile species that may be dissolved in magma at a particular set of pressure, temperature, melt composition and oxygen fugacity conditions (e.g., Burgisser et al., 2015; Duan, 2014; Scaillet & Pichavant, 2005). At equilibrium, the fugacity of each volatile species in the melt is equal to its fugacity in the fluid (Scaillet & Pichavant, 2005), such that a fraction of volatiles are dissolved in magma and the remainder are exsolved in the gas phase. Since magmatic volatiles are less soluble at low pressure, magma decompression is a principal driver for volatile exsolution (e.g., Burgisser et al., 2015; Duan, 2014; Papale, 1999).

Thermodynamic models based on mass balance and equilibrium constants may be used to calculate the mass and composition of the exsolved volatile phase in the chamber and this may be then used to estimate bulk magma properties such as density and compressibility (Gaillard & Scaillet, 2014; Ohmoto & Kerrick, 1977). The concentration of each volatile species exsolved at any given pressure and temperature can be calculated using its corresponding solubility laws (e.g., Burgisser et al., 2015). Here, we use the Python degassing model EVo, as implemented in EVolve (Liggins et al., 2020, 2021), which uses the H_2O and CO_2 solubility constants from Burgisser et al. (2015), along with the sulfide capacity law of O'Neill (2021) and the sulfate solubility model of

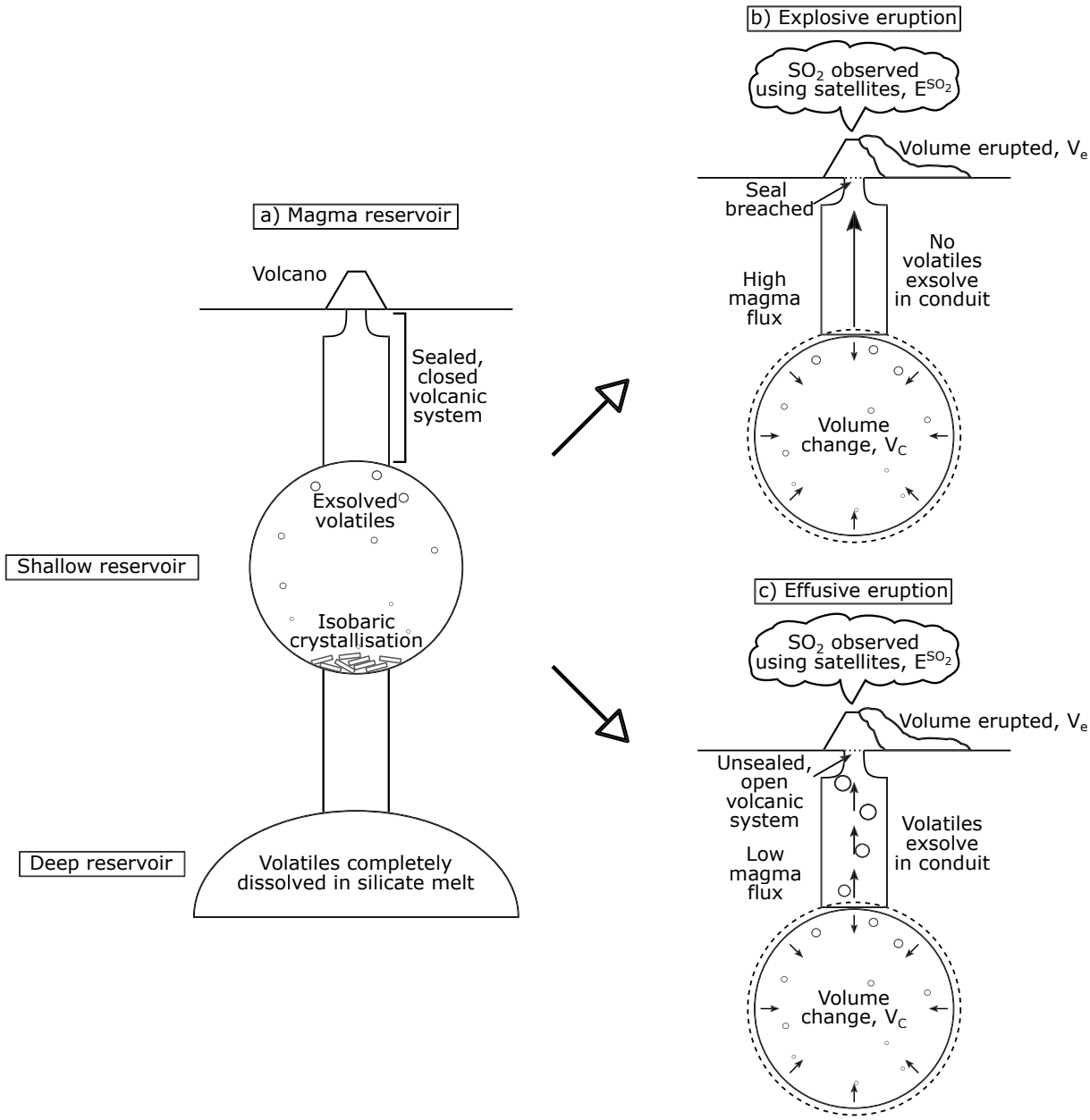

Figure 1. Conceptual model of magma degassing during eruptions of different styles. (a) Volcano with chambers at different depths, prior to an eruption. Magmatic volatiles are more soluble in deep magmatic chambers and thus a higher proportion of the total volatile load will be dissolved in the silicate melt. In the shallow chamber (at a lower pressure) there is a higher proportion of exsolved volatiles, with degassing being driven both by decompression as magma moves up from the lower chamber, and by isobaric cooling and crystallisation. (b) During explosive eruptions of silicic magmas, magma is removed from the chamber and decompressed rapidly, with little volatile exsolution during magma ascent. Much of the volatiles emitted as gases during the eruption represents a pre-eruptive exsolved volatile phase that was present in the chamber prior to decompression (and which made the magma compressible). In this "explosive" case we expect the volume change inferred from ground deformation at the surface to be related to the amount of volatiles emitted during eruption (both normalized by erupted volume). (c) Effusive eruptions, on the other hand, are characterized by a low magma ascent rate between the chamber and the surface, allowing extensive volatile exsolution in the conduit, that is, co-eruptive degassing. The volcanic gases observed at the surface are mostly derived from decompressional degassing and do not constrain the compressibility of the chamber. In this "effusive" case, we do not expect a relationship between the amount of gases released during the eruption and the volume change inferred for the "source" chamber during eruption.

Nash et al. (2019), to predict the physicochemical properties of basaltic magma, such as the composition of the gas phase and magma density, as a function of melt composition, magmatic volatile content, oxygen fugacity of magma, temperature and pressure. We note there are limitations in this model for predicting sulfur behavior, in that it uses the sulfide capacity law of O'Neill (2021) that is more appropriate for sulfur in more reduced melts

15252027, 2022, 7, Downloaded from https://agupubs.onlinelibrary.wiley.com/doi/10.1029/2022GC010387 by Alaska State Library, Wiley Online Library on [23/06/2025]. See the Terms and Conditions (https://onlinelibrary.wiley.com/terms-and-conditions) on Wiley Online Library for rules of use; OA articles are governed by the applicable Creative Commons License

15252027, 2022, 7, Downloaded from https://agupubs.onlinelibrary.wiley.com/doi/10.1029/2022GC010387 by Alaska State Library, Wiley Online Library on [23/06/2025]. See the Terms and Conditions (https://onlinelibrary.wiley.com/terms-and-conditions) on Wiley Online Library for rules of use; OA articles are governed by the applicable Creative Commons License

than those considered here, and the lack of sulfate capacity law that limits the accuracy of the model at high f_{O_2} conditions (Liggins et al., 2020, 2021).

We use EVo to calculate magma and fluid compositions in the C-O-H-S-Fe system during magma decompression (Liggins et al., 2020, 2021). We initialize the model using the weight fraction of the volatile species H_2O, CO_2 and S as input parameters. The oxygen fugacity (f_{O_2}) is adjusted relative to the Ni-NiO buffer (NNO). EVo can be initialized by either 1) specifying starting pressure (p), and gas weight fraction (w_g), or 2) calculating the saturation pressure for the given composition (i.e., $w_g \approx 0$ wt%). Here we use the saturation point based on melt composition to find an appropriate starting pressure/depth (Liggins et al., 2021). We do not consider the processes of crystallisation or magma recharge implicitly in our model, for simplicity.

At a specified depth, the gas volume fraction (V_g) is controlled by the total gas weight fraction (w_g) and gas density (ρ_g):

$$V_g = \left(1 + \frac{M P (1 - w_g)}{R T \rho_M w_g}\right)^1, \tag{1}$$

where M is the average molar mass of the gas phase, R is the universal gas constant (8.31 J mol^{-1} K^{-1}) and ρ_M is the volatile-free magma density (e.g., Burgisser et al., 2015). Magma density (ρ_m) is a function of the density and volume fraction of both melt and gas (Spera, 2000):

$$\rho_m = \rho_g V_g + \rho_M (1 - V_g). \tag{2}$$

V_g increases during magma decompression and hence decreases ρ_m. Since ρ_m changes with p, magma compressibility (β_m) can be linked to the density and density gradient of magma with respect to pressure (Huppert & Woods, 2002):

$$\beta_m = \frac{1}{\rho_m}\frac{\delta \rho_m}{\delta p}. \tag{3}$$

Given how ρ_m changes with V_g, magma compressibility is dominated by the weight fraction of exsolved gas phase and hence magmatic volatile content (Edmonds et al., 2018; Kilbride et al., 2016).

Permeability develops when gas bubbles coalesce to form porous networks, thereby allowing exsolved volatiles to percolate through magma efficiently (Bachmann & Bergantz, 2006; Candela, 1997; Collins et al., 2009; Lindoo et al., 2017; Lowenstern, 1994). Magma becomes permeable when it reaches critical porosity, which is also defined as the percolation threshold (ϕ_c). In this study, we use gas volume fraction (V_g) to represent magma porosity and assume that magma becomes permeable and degasses as it reaches the percolation threshold. The value of ϕ_c is widely variable, ranging from ~17–78 vol%, due to the complex interplay between magma properties and physical processes such as melt viscosity and decompression rate (Burgisser et al., 2017; Colombier et al., 2020; Rust & Cashman, 2011). For melts with low viscosity and overpressure, such as the basaltic melts considered here, bubbles can grow and rise buoyantly, which reduce the likelihood of the bubbles coalescing to form a porous network. Colombier et al. (2020) suggest that low viscosity melts would become permeable at $\phi_c > 37$ vol% and we use that threshold here.

3.2. Linking Magma Properties to Observable Parameters

3.2.1. Deformation

Observations of subsurface volume change (derived from inverting measurements of surface deformation) may be compared to the model of magma properties during degassing. We define the normalized volume change, $\bar{V}$, as the ratio between the subsurface volume change (ΔV_c) and the volume erupted (V_e; assuming dense-rock equivalent, DRE):

$$\bar{V} = \frac{\Delta V_c}{V_e} = \left(1 + \frac{\beta_m}{\beta_c}\right)^{-1}, \tag{4}$$

15252027, 2022, 7, Downloaded from https://agupubs.onlinelibrary.wiley.com/doi/10.1029/2022GC010387 by Alaska State Library, Wiley Online Library on [23/06/2025]. See the Terms and Conditions (https://onlinelibrary.wiley.com/terms-and-conditions) on Wiley Online Library for rules of use; OA articles are governed by the applicable Creative Commons License

where β_m is magma compressibility and β_c is chamber compressibility (Kilbride et al., 2016; Rivalta & Segall, 2008). Note that the definition of $\bar{V}$ is the inverse of that from Kilbride et al. (2016), that is, $r = \bar{V}^{-1}$. In an elastic half-space, chamber compressibility is affected by host rock properties and chamber geometry, which can be defined as

$$\text{Spherical point source:} \quad \beta_c = \frac{3}{4\mu} \tag{5}$$

$$\text{Prolate chamber:} \quad \beta_c = \frac{1}{\mu} \tag{6}$$

$$\text{Horizontal oblate ellipsoid (sill):} \quad \beta_c = \frac{1}{\mu}\left(\frac{a}{c}\frac{3}{2\pi} - \frac{3}{5}\right) \tag{7}$$

where μ is the shear modulus of the crust and $\frac{a}{c}$ is the ratio of major to minor semi-axes of an oblate ellipsoid (Amoruso & Crescentini, 2009; Anderson & Segall, 2011).

For compressible magmas, ΔV_c would be less than V_e (i.e., $\bar{V} < 1$), such that compressible magmas with low β_c/β_m have low volume change per unit erupted (Voight et al., 2010), while ΔV_c would be approximately equal to V_e (i.e., $\bar{V} \approx 1$) for incompressible magmas and high β_c/β_m. Since chamber geometry and host rock properties also affect β_c and hence the magnitude of $\bar{V}$, volcanoes with compressible magmas and rigid surrounding crust (i.e., high μ and low β_c) cause small volume changes during an eruption (Kilbride et al., 2016; Rivalta & Segall, 2008).

A directly observable parameter is surface deformation. Here we define normalized displacement $\bar{z}$ as the maximum vertical displacement per unit volume erupted (i.e., located directly above the source). For simplicity, we only calculate the normalized displacement for a spherical point source in a uniform and elastic half-space (Mogi, 1958), $\bar{z} = \bar{V}\,\frac{1-\upsilon}{\pi}\,\frac{1}{d^2}$, where υ is Poisson's ratio and d is the depth of magma chamber, although other models are also available (e.g., Albino et al., 2019; Fialko et al., 2001; Masterlark, 2003; Okada, 1985; Yang et al., 1988; Zhan et al., 2019).

3.2.2. Degassing

Observations of SO_2 degassing are made by satellite-based sensors (e.g., Carn et al., 2016; Prata & Kerkmann, 2007; Theys et al., 2019). We define normalized SO_2 $(\bar{S})$ as the observed SO_2 emitted (E^{SO_2}), normalized by the volume of magma erupted (V_e). $\bar{S}$ estimates the mass of SO_2 per unit volume of magma:

$$\bar{S} = \frac{E^{SO_2}}{V_e} = \frac{m^{SO_2} M^{SO_2} \rho_e w_g}{M_g}, \tag{8}$$

where m^{SO_2} is the mole fraction of SO_2 in gaseous phase, M^{SO_2} is the molecular mass of SO_2, $\rho_e = 2800$ kg m^{-3} is the erupted rock density typical for basalts (Stolper & Walker, 1980; Wu et al., 2020), and M_g is the mean molecular mass of the gas phase. We consider all sulfur species in the degassing model, but we extract the SO_2 flux to compare to observations. For explosive eruptions, we assume that the mass of SO_2 emissions at the surface (E^{SO_2}) is the same as the mass of SO_2 in equilibrium with magma at chamber depth, meaning that there is no additional degassing as magma rises from the chamber to the surface (Figure 1b). For effusive eruptions, volatiles exsolve in the conduit as magma ascends slowly such that SO_2 degassing is dominated by co-eruptive degassing (Figure 1c). For simplicity, we assume all exsolved SO_2 is emitted as SO_2 in the plume (i.e., there are no other sulfur-bearing species present) and that all SO_2 can be detected by satellites. We ignore sulfur loss due to leaching, sulfur scrubbing by hydrothermal systems, and the formation of sulfide globules during sulfide saturation. We note that these assumptions may break down during some eruptions, which has been demonstrated for the 2011 eruption of Grimsvötn (Sigmarsson et al., 2013) and the 2018 eruption of Kīlauea (Wieser et al., 2020).

4. One-at-a-Time Sensitivity Tests

In this section, we explore the sensitivity of the calculated magma properties to initial magmatic H_2O content (w^{H_2O}), magmatic CO_2 content (w^{CO_2}), oxygen fugacity (f_{O_2}), magmatic S content (w^S), crustal shear modulus (μ) and chamber geometry. We conduct one-at-a-time sensitivity tests by holding other parameters constant

15252027, 2022, 7, Downloaded from https://agupubs.onlinelibrary.wiley.com/doi/10.1029/2022GC010387 by Alaska State Library, Wiley Online Library on [23/06/2025]. See the Terms and Conditions (https://onlinelibrary.wiley.com/terms-and-conditions) on Wiley Online Library for rules of use; OA articles are governed by the applicable Creative Commons License

Table 2
Summary of Sensitivity Tests Showing the Greatest Percentage Change of Each Observation and the Depth at Which It Occurred

Parameters	% Change in normalized SO_2, $\bar{S}$	Depth (km)	% Change in normalized volume change, $\bar{V}$	Depth (km)	% Change in normalized displacement, $\bar{z}$	Depth (km)
Magmatic H_2O, w^{H_2O} (1.0–3.0 wt%)	+170%	0.51 km	−68%	3.5 km	−83%	1.8 km
Magmatic CO_2, w^{CO_2} (1000–5000 ppm)	+180%	1.5 km	−53%	3.3 km	−58%	2.8 km
Oxygen fugacity, f_{O_2}(NNO − 1-NNO + 2)	+183%	surface	+4.3%	3.7 km	+4.8% 4.2 km	
Magmatic S, w^S (1000–3000 ppm)	+109%	surface	<−1.0%	surface	<−1.0%	surface
Crustal shear modulus, μ (0.1–30 GPa)	n/a	n/a	−94%	4 km	−100%	surface

Note. To conduct the sensitivity tests, we increase the value of each parameter (shown in brackets) while holding other parameters constant. For example, when increasing H_2O wt% from 1.0 to 3.0, initial CO_2, S, fo_2 and μ are kept constant. Please refer to Table 1 for details of the parameter space.

and varying the chosen parameter. The ranges in each parameter were chosen to represent the natural variation within typical basalts (45%–52% SiO_2). For each example, we first consider the general sensitivity of the model to changing magma properties by looking at the greatest percentage changes over a range of depths, and then provide an illustrative example for a chamber at a depth of 5 km (i.e., pressure of 137 MPa). While this provides a clear understanding of the role of each parameter, it does not consider the co-dependence of input variables, which may result in parameter combinations that are not physically realistic.

Bulk magma volatile contents are informed by observations of dissolved volatile content from melt inclusions of basalts. For simplicity, we assume an isothermal magma at 1200°C. We use values of w^{H_2O}, w^{CO_2} and w^S that are typical for basaltic magmas (e.g., Wallace, 2005; Ruscitto et al., 2012; Plank et al., 2013), in the ranges of 1.0–3.0 wt% H_2O, 1000–5000 ppm CO_2, and 1000–3000 ppm S, respectively (Table 1). We use f_{O_2} from NNO−1 to NNO+2, which are calibrated for basaltic systems (Konecke et al., 2019), to explore the effects of oxygen fugacity on the solubility of volatile species. Since f_{O_2} has a minimal effect on both H_2O and CO_2 concentrations over the range we consider, we expect that varying f_{O_2} will primarily affect the proportions of H_2S and SO_2 in the vapor phase.

To test how chamber compressibility (β_c) affects volcanic deformation, we use μ from 0.1 to 30 GPa (Heap et al., 2020), and consider three chamber geometries: a spherical point source, a vertical prolate ellipsoid (pipe-like chamber) and a horizontal oblate ellipsoid (sill) (A. Gudmundsson, 2008; Amoruso & Crescentini, 2009; Anderson & Segall, 2011). Although we do not expect the gas to remain in contact with the magma when V_g exceeds the percolation threshold at which magma becomes permeable, that is, $\phi_c > 37$ vol% (Colombier et al., 2020), we run our sensitivity tests all the way to the surface. This is because basaltic magmas have high volatile diffusivities due to high temperature and the sulfur left dissolved in the melt may continue to exsolve during ascent such that the actual amount of SO_2 emitted is in equilibrium with surface pressure. Table 2 summarizes the greatest percentage change over the depth range of each parameter for the estimated values of $\bar{S}$, $\bar{V}$ and $\bar{z}$.

4.1. Effects of H_2O Content on Magma Properties

First, we vary the initial dissolved H_2O content (w^{H_2O}) in the melt and investigate how it affects magma properties ρ_m and β_m, and observables $\bar{S}$, $\bar{V}$ and $\bar{z}$ (Figure 2). In this sensitivity test, w^{H_2O} ranges from 1.0 to 3.0 wt% and the constant parameters are $w^{CO_2} = 3000$ ppm, $f_{O_2} =$ NNO, $w^S = 2000$ ppm. We assume a fixed chamber compressibility for a spherical cavity (Equation 5) where $\mu = 2.1$ GPa (i.e., $\beta_c = 3.6 \times 10^{-10}$ Pa^{-1}).

Solubility decreases with decreasing pressure for each volatile component, so as pressure decreases, the mass fraction dissolved in the melt $\left(w_M^x\right)$ decreases and the mole fraction that has exsolved to the gaseous phase $\left(m_g^x\right)$ increases (Figures 2a and 2b). Higher w^{H_2O} reduces the solubility of CO_2 and S (Figure 2a), thus increasing the mole fraction of $m_g^{H_2O}$, $m_g^{CO_2}$ and m_g^S (Figure 2b). Normalized SO_2 $\left(\bar{S}\right)$ represents the mass of exsolved SO_2 per unit volume of magma, assuming that the exsolved SO_2 remains in the bulk magma and does not segregate. By increasing w^{H_2O} by a factor of 3, $\bar{S}$ increases up to a maximum of ∼170% at 0.51 km depth (Figure 2c). Gas volume fraction (V_g) increases as volatiles exsolve and gas bubbles expand at lower pressures. Since V_g is

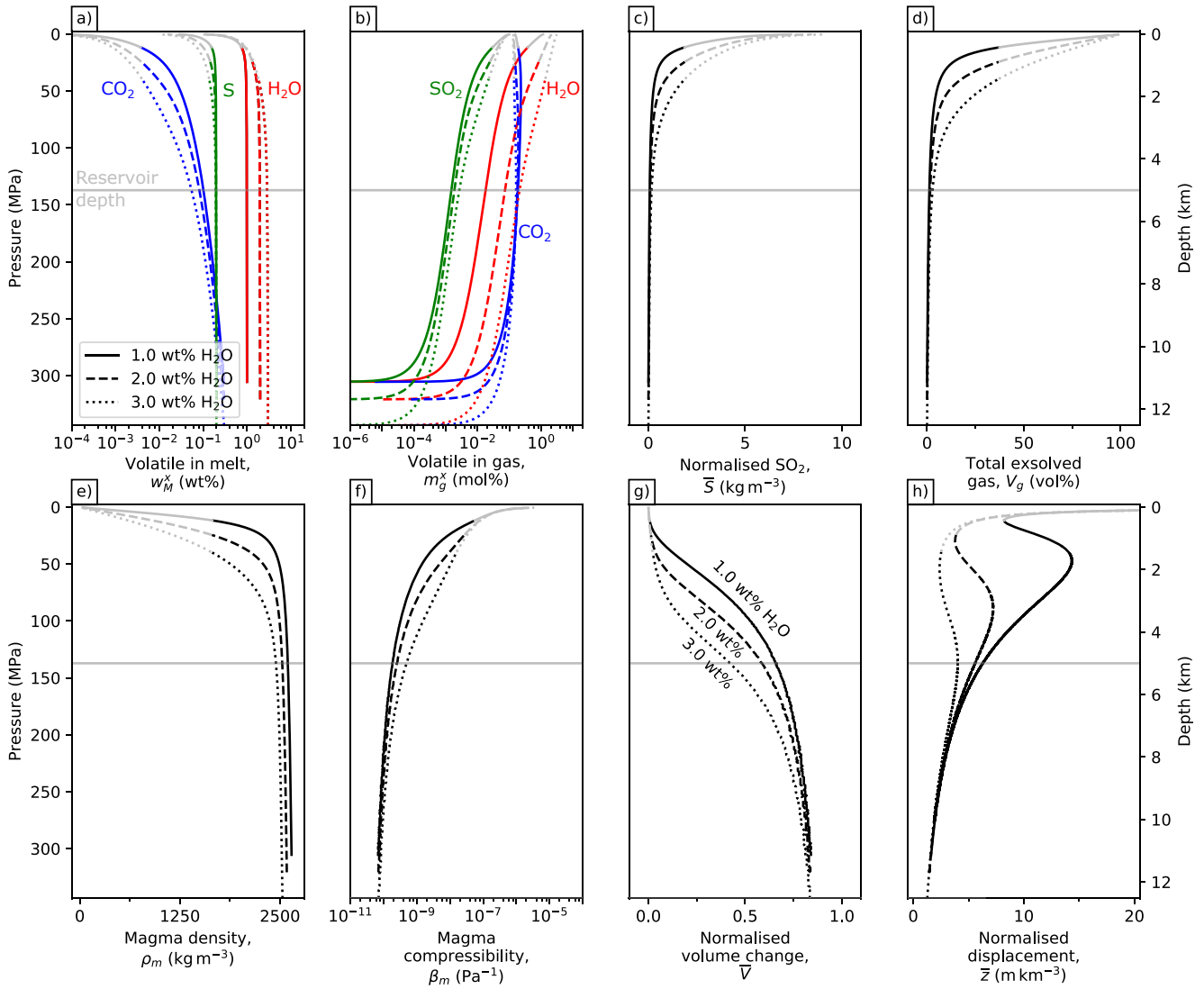

Figure 2. Physicochemical properties of basalts when varying the initial magmatic H_2O from 1.0 to 3.0 wt%. (a) Weight fraction of dissolved H_2O, CO_2 and S in melt $\left(w_M^x\right)$. (b) Mole fraction of exsolved H_2O, CO_2 and SO_2 in gas $\left(m_g^x\right)$. (c) Mass of SO_2 gas per unit volume of magma, also defined as normalized SO_2 $\left(\overline{S}\right)$. (d) Volume fraction of exsolved gases in magma (V_g). (e) Magma density (ρ_m). (f) Magma compressibility (β_m). (g) Model predicted volume change normalized by unit volume of magma $\left(\overline{V}\right)$. (h) Maximum vertical displacement normalized by unit volume of magma $(\bar{z})$. Panels a, b, d and e show magma properties as a function of depth and panels c, g and h represent the model value for a unit volume of magma that instantaneously erupted from a particular depth. The gray lines represent magma properties after exceeding percolation threshold $\phi_c = 37$ vol%. Fixed parameters: $w^{CO_2} = 3000$ ppm, $f_{O_2} = \text{NNO}$, $w^S = 2000$ ppm and $\mu = 2.1$ GPa.

dominated by w^{H_2O}, V_g increases up to a maximum of ~210% at 0.65 km depth when increasing w^{H_2O} from 1.0 to 3.0 wt% (Figure 2d).

The increase in w^{H_2O} increases V_g, which decreases magma density (ρ_m; Equation 2; Figure 2e) and increases magma compressibility (β_m; Equation 3; Figure 2f). Therefore, with the increase of w^{H_2O} from 1 to 3 wt%, β_m increases up to a maximum of ~650% at 2.1 km depth (Figure 2f), and normalized volume change $\left(\overline{V}\right)$ decreases up to a maximum of ~68% at 3.5 km depth (Figure 2g). Based on the simple Mogi model, there is a trade-off between volume change and depth, such that the same volume change will cause a larger displacement at a shallow depth. However, when V_g and β_m are considered, the maximum vertical displacement per unit volume $(\bar{z})$ does not vary in a simple way; the increase in V_g toward the surface causes a local minimum in $\bar{z}$ at 0.5 km depth. Given that $\bar{z}$ is controlled by chamber depth and $\overline{V}$, increasing w^{H_2O} thus causes a relative decrease in the normalized displacement $(\bar{z})$ up to a maximum of ~83% at 1.8 km depth (Figure 2h).

15252027, 2022, 7, Downloaded from https://agupubs.onlinelibrary.wiley.com/doi/10.1029/2022GC010387 by Alaska State Library, Wiley Online Library on [23/06/2025]. See the Terms and Conditions (https://onlinelibrary.wiley.com/terms-and-conditions) on Wiley Online Library for rules of use; OA articles are governed by the applicable Creative Commons License

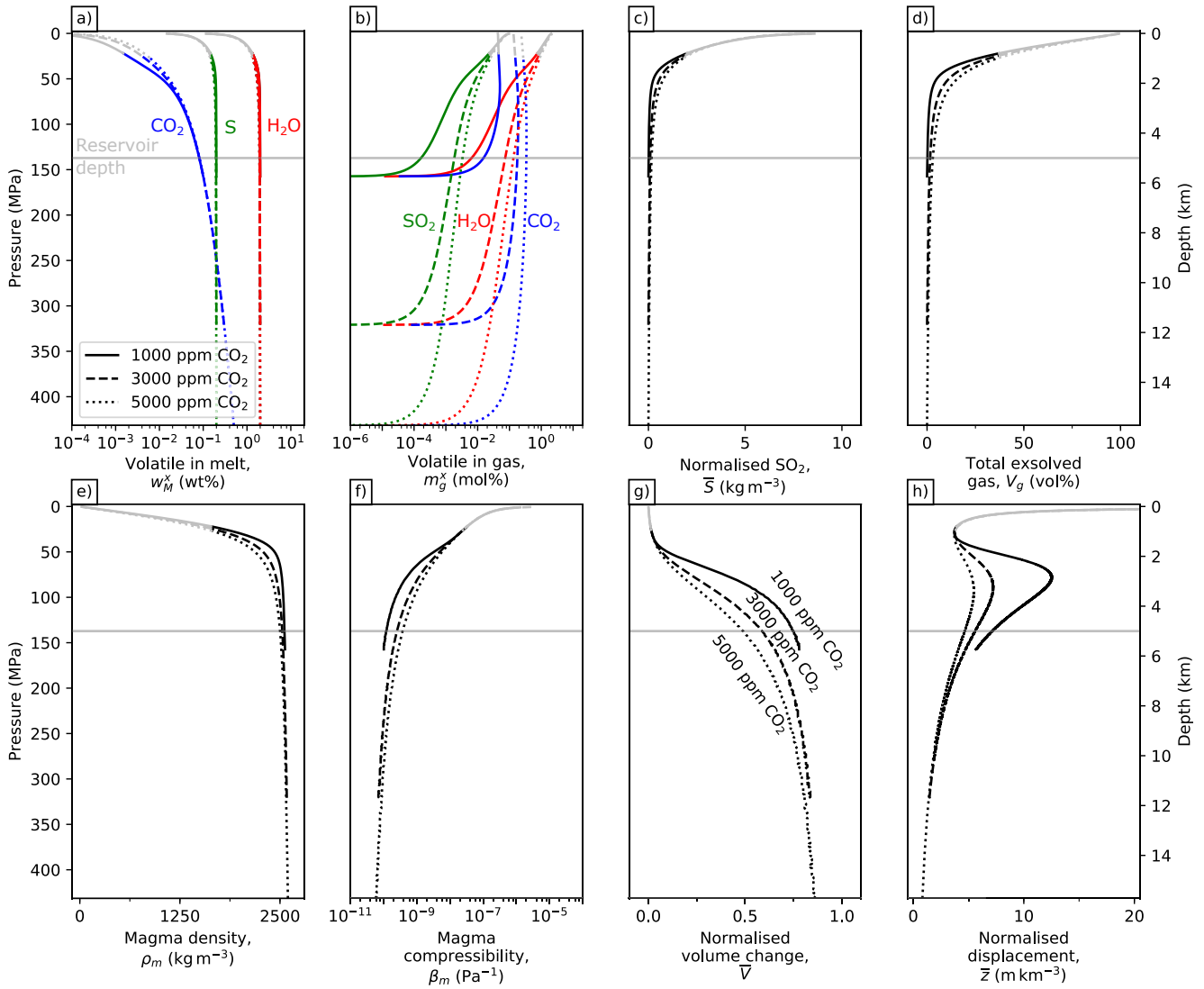

Figure 3. Physicochemical properties of basalts when varying the initial weight fraction of dissolved CO_2 (w^{CO_2}) from 1000 to 5000 ppm. Same general format as for Figure 2. Fixed parameters: (w^{H_2O}) = 2.0 wt%, f_{O_2} = NNO, w^S = 2000 ppm and μ = 2.1 GPa.

To illustrate these results, we give specific values for a chamber depth of 5 km. Varying w^{H_2O} from 1.0 to 3.0 wt% increases $\bar{S}$ from 0.064 kg m^{-3} to 0.16 kg m^{-3} (Figure 2c). V_g increases from 1.2 vol% to 2.8 vol%, which corresponds to the increase in β_m from 1.9×10^{-10} Pa^{-1} to 4.9×10^{-10} Pa^{-1} (Figure 2f). As a result, $\bar{V}$ decreases from 0.65 to 0.42 (Figure 2g) and $\bar{z}$ is reduced from 6.3 m km^{-3} to 4.0 m km^{-3} (Figure 2h). The model thus predicts that basalts with high initial H_2O content have high $\bar{S}$ and β_m, and as a result, low $\bar{V}$ and $\bar{z}$ (Figure 2).

4.2. Effects of CO_2 Content on Magma Properties

Here, we vary the initial dissolved CO_2 content in the magma to understand how it affects magma properties and observables $\bar{S}$, $\bar{V}$ and $\bar{z}$ (Figure 3). We use w^{CO_2} in the range of 1000–5000 ppm and fixed (w^{H_2O}) = 2.0 wt%, f_{O_2} = NNO, w^S = 2000 ppm and μ = 2.1 GPa for this model.

Figure 3a shows that increasing w^{CO_2} from 1000 to 5000 ppm increases the amount of dissolved $w_M^{CO_2}$ up to a maximum of 73% at 1.5 km depth, but decreases $w_M^{H_2O}$ and w_M^S by <12% and <11%, respectively. This results in a relative increase in the amount of exsolved SO_2 $\left(m_g^{SO_2}\right)$ and $\bar{S}$ up to a maximum of ~120% and ~180%, respec-

15252027, 2022, 7, Downloaded from https://agupubs.onlinelibrary.wiley.com/doi/10.1029/2022GC010387 by Alaska State Library, Wiley Online Library on [23/06/2025]. See the Terms and Conditions (https://onlinelibrary.wiley.com/terms-and-conditions) on Wiley Online Library for rules of use; OA articles are governed by the applicable Creative Commons License

15252027, 2022, 7, Downloaded from https://agupubs.onlinelibrary.wiley.com/doi/10.1029/2022GC010387 by Alaska State Library, Wiley Online Library on [23/06/2025]. See the Terms and Conditions (https://onlinelibrary.wiley.com/terms-and-conditions) on Wiley Online Library for rules of use; OA articles are governed by the applicable Creative Commons License

tively, at 1.5 km depth (Figures 3b and 3c). Similarly, varying initial CO_2 content increases V_g up to a maximum of ~110% at 1.5 km depth (Figure 3d). Increasing w^{CO_2} corresponds to an increase in β_m up to a maximum of <250% and a decrease in $\bar{V}$ up to a maximum of 53% at 3.3 km depth (Figures 3f and 3g), which correlates to the decrease in $\bar{z}$ up to a maximum of 58% at 2.8 km depth (Figure 3h).

Here, we quantify these results for a depth of 5 km to illustrate the sensitivity to w^{CO_2}. Increasing initial CO_2 from 1000 to 5000 ppm increases $\bar{S}$ from 0.0082 kg m^{-3} to 0.163 kg m^{-3} and V_g from 0.14 vol% to 3.0 vol% (Figures 3c and 3d). This corresponds to an increase in β_m from 1.2×10^{-10} Pa^{-1} to 3.8×10^{-10} Pa^{-1} (Figure 3f). As a result, $\bar{V}$ decreases from 0.75 to 0.49 (Figure 3g) and $\bar{z}$ is reduced from 7.2 m km^{-3} to 4.7 m km^{-3} (Figure 3h). The model shows that increasing initial CO_2 content from 1000 to 5000 ppm causes significant changes to both $\bar{V}$ and $\bar{z}$, similar to that of varying initial H_2O content from 1.0 wt% to 3.0 wt%.

4.3. Effects of Sulfur Content on Magma Properties

Here, we vary initial dissolved sulfur (S) content to understand how it affects magma properties and observables $\bar{S}$, $\bar{V}$ and $\bar{z}$ (Figure 4). We use w^S in the range of 1000 ppm–3000 ppm and fixed $w^{H_2O} = 2.0$ wt%, $w^{CO_2} = 3000$ ppm, $f_{O_2} =$ NNO and $\mu = 2.1$ GPa for this model.

Figure 4a shows that w_M^S increases by <200% at ~12 km depth with increasing w^S from 1000 ppm to 3000 ppm, which corresponds to the increase in $m_g^{SO_2}$ and $\bar{S}$ up to a maximum of ~122% and ~109% at the surface, respectively (Figures 4b and 4c). The total gas volume fraction, however, increases by only <3.7% at 1 km depth (Figure 4d). Since varying initial S content has minimal impact on V_g, β_m only increases by <0.24% at surface depth (Figure 4f), which results in <1% decrease in both $\bar{V}$ and $\bar{z}$ (Figures 4g and 4h).

We quantify these results for a depth of 5 km to illustrate the effect of varying w^S from 1000 ppm to 3000 ppm. This range of sulfur is less than the sulfur content at sulfide saturation. Increasing magmatic w^S increases $\bar{S}$ from 0.045 kg m^{-3} to 0.14 kg m^{-3} (Figure 4c), which is so minimal that V_g remains constant 1.6 vol% despite increasing w^S from 1000 ppm to 3000 ppm (Figure 4d). This corresponds to indistinguishable changes in β_m at 2.5×10^{-9} Pa^{-1} (Figure 4f). As such, both $\bar{V}$ and $\bar{z}$ are 0.59 and 5.6 m km^{-3}, respectively (Figures 4g and 4h). The model shows that basalts with high initial w^S release high $\bar{S}$ but β_m and hence co-eruptive deformation is only minimally affected.

4.4. Effects of Oxygen Fugacity on Magma Properties

Figure 5 shows how varying oxygen fugacity (f_{O_2}) affects magma properties, and consequently observables $\bar{S}$, $\bar{V}$ and $\bar{z}$. We vary f_{O_2} from NNO−1 to NNO+2 and fix $w^{H_2O} = 2.0$ wt%, $w^{CO_2} = 3000$ ppm, $w^S = 2000$ ppm and $\mu = 2.1$ GPa for this model.

The model predicts that varying f_{O_2} from NNO−1 to NNO+2 increases $w_M^{CO_2}$, $w_M^{H_2O}$ and w_M^S up to a maximum of 2.2%, 6.6% and 21%, respectively, at 1 km depth, because f_{O_2} is primarily affecting the fugacities of H_2S and SO_2 in the gas phase and only indirectly affects H_2O and CO_2 as a result. (Figure 5a). The significant increase in w_M^S causes a relative increase $m_g^{SO_2}$ and $\bar{S}$ up to a maximum of 176% and 183%, respectively, at surface depth (Figures 5b and 5c).

However, V_g is reduced by only <7% at 2.8 km depth so varying f_{O_2} has minimal impact on ρ_m and β_m (Figure 5e). In fact, increasing f_{O_2} from NNO−1 to NNO+2 decreases β_m by 6.9% at 3.6 km depth (Figure 5f) and hence $\bar{V}$ of oxidized basalts is <4.3% greater than its reduced counterpart at 3.7 km depth (Figure 5g). While $\bar{z}$ is controlled by chamber depth and $\bar{V}$, the maximum increase in $\bar{z}$ of less than 4.8% also occur at 4.2 km depth due to insignificant difference in $\bar{V}$ when varying f_{O_2} (Figure 5h).

Next, we quantify the predictions for a depth of 5 km. Varying f_{O_2} from NNO−1 to NNO+2 increases $\bar{S}$ from 0.020 kg m^{-3} to 0.077 kg m^{-3} (Figure 5c). However, V_g decreases from 1.6 vol% to 1.5 vol%, which corresponds to a decrease in β_m from 2.6×10^{-10} Pa^{-1} to 2.5×10^{-10} Pa^{-1} (Figure 5f). As a result, $\bar{V}$ and $\bar{z}$ increases from

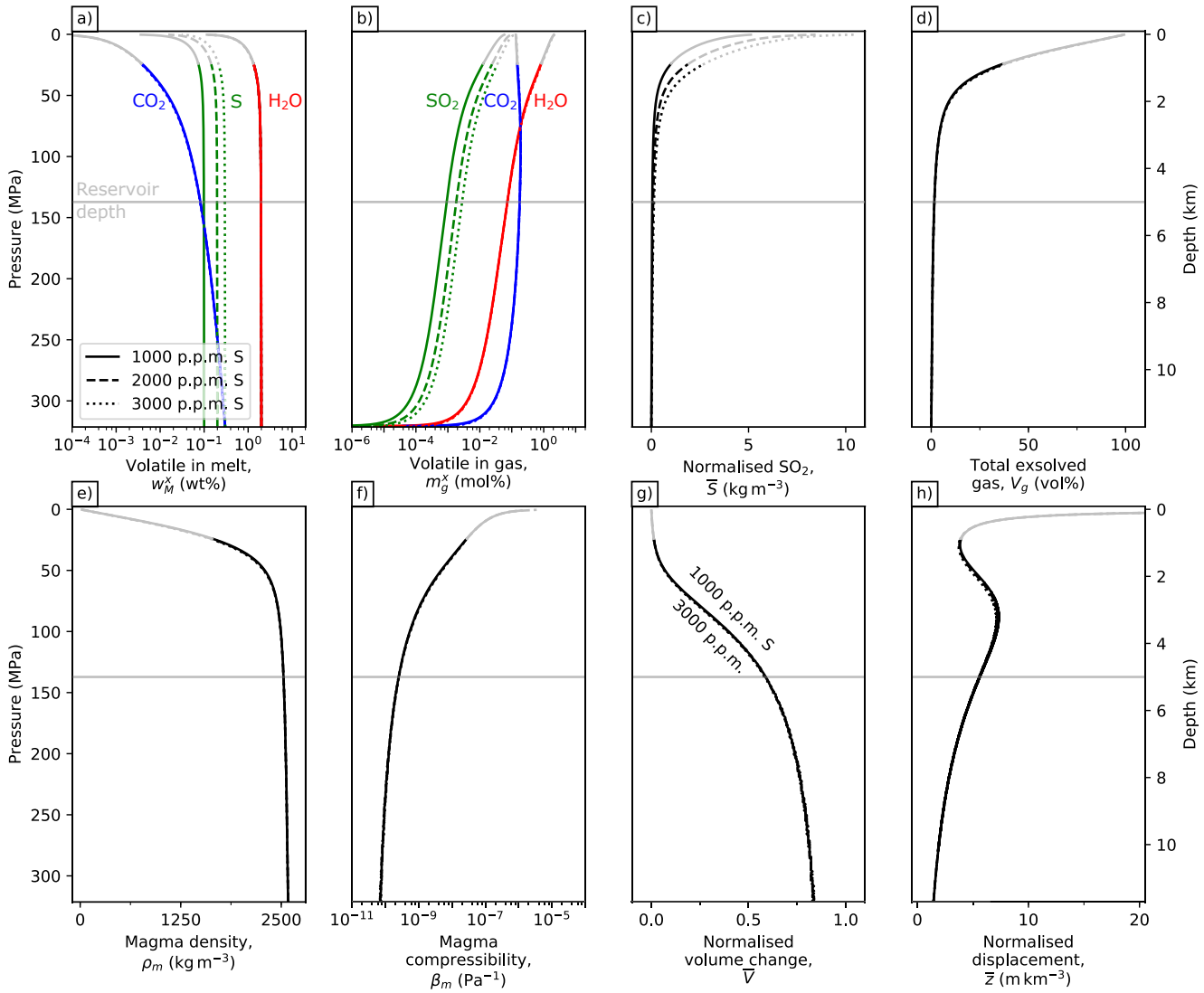

Figure 4. Physicochemical properties of basalts when varying the initial weight fraction of dissolved S (w^S) from 1000 to 3000 ppm. Same general format as for Figure 2. Fixed parameters: $w^{H_2O} = 2.0$ wt%, $w^{CO_2} = 3000$ ppm, f_{O_2} = NNO and $\mu = 2.1$ GPa.

0.58 to 0.59 and 5.5 m km^{-3} to 5.6 m km^{-3}, respectively (Figures 5g and 5h). The model thus predicts that while oxidized basalts have greater $\bar{S}$ than reduced basalts, variations in oxygen fugacity of basalts has minimal impact on co-eruptive deformation.

4.5. Effects of Chamber Compressibility

Crustal properties and chamber geometry are known to have a major role in determining surface deformation (e.g., A. Amoruso & Crescentini, 2009; Anderson & Segall, 2011; Gudmundsson, 2008; Heap et al., 2020). Here we investigate the two parameters that directly affect our simplified model using the same sensitivity analysis as for the other parameters. $\bar{V}$ is a function of β_m and β_c, and the two parameters we explore in this section are crustal shear modulus and chamber geometry that control β_c (Equation 4). We use a range of crustal shear modulus (μ) from 0.1 GPa (compliant crust) to 30 GPa (non-compliant crust), which is typical in volcanic areas (A. Gudmundsson, 2005; Rivalta & Segall, 2008). It is noted that μ depends primarily on porosity and hence degree of fracturing of the host rock (Heap et al., 2020), which does not vary systematically with tectonic setting. μ changes with depth but for simplicity, we assume a constant μ at all depths. We considered three representative chamber geometries, which are a spherical point source, a vertical prolate ellipsoid (pipe-like chamber) and a

15252027, 2022, 7, Downloaded from https://agupubs.onlinelibrary.wiley.com/doi/10.1029/2022GC010387 by Alaska State Library, Wiley Online Library on [23/06/2025]. See the Terms and Conditions (https://onlinelibrary.wiley.com/terms-and-conditions) on Wiley Online Library for rules of use; OA articles are governed by the applicable Creative Commons License

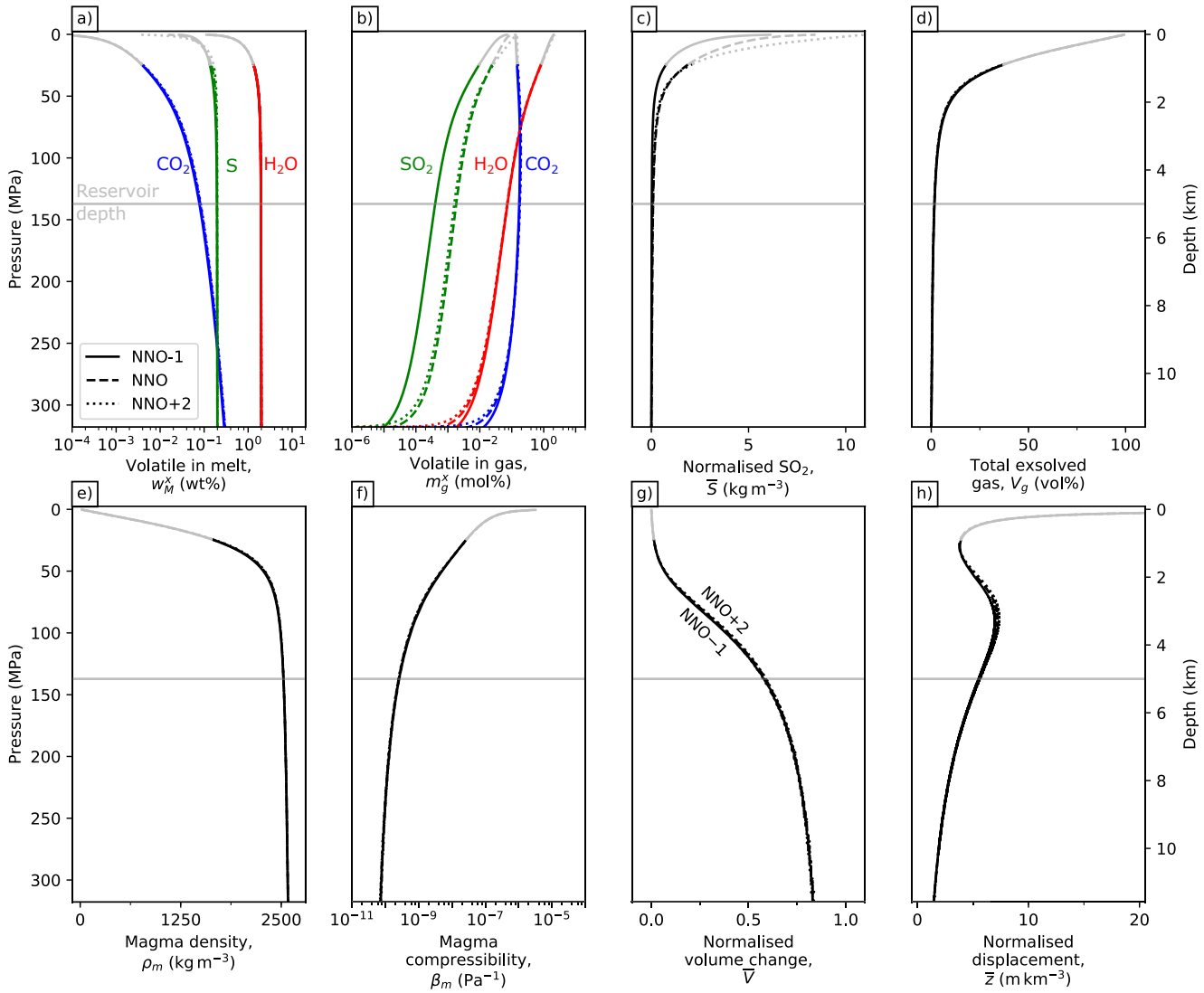

Figure 5. Physicochemical properties of basalts when varying f_{O_2} of magma storage from NNO−1 to NNO+2. Same general format as for Figure 2. Fixed parameters: $w^{H_2O} = 2.0$ wt%, $w^{CO_2} = 3000$ ppm, $w^S = 2000$ ppm and $\mu = 2.1$ GPa.

horizontal oblate ellipsoid (sill), and use $\frac{a}{c} = 100$ for the horizontal sill (Equation 5; Amoruso & Crescentini, 2009; Anderson & Segall, 2011). We use a Poisson's ratio v of 0.30 based on the average value for volcanic rock with average porosity and fracture density (Heap et al., 2020). The sensitivity test uses fixed parameters of $w^{H_2O} = 2.0$ wt%, $w^{CO_2} = 3000$ ppm, $f_{O_2} = $ NNO, and $w^{H_2O} = 2000$ ppm.

To understand how crustal properties affect volcanic deformation, we first discuss the effects of μ and chamber geometry on the ratio of β_c/β_m. Since β_c is inversely proportional to μ, a crust with $\mu = 0.1$ GPa results in $\beta_c/\beta_m = 30$ for a chamber at 5 km depth, while $\beta_c/\beta_m = 0.099$ for a crust with $\mu = 30$ GPa (Figure 6a). From Equation 5, the crustal compressibility β_c for chambers with a vertical pipe-like shape is 33% higher than a spherical point source and thus increases the β_c/β_m of a vertical pipe-like chamber by 33% when compared to that of a spherical point source (Figure 6b). An ellipsoid with $\frac{a}{c} = 100$ has the highest β_c among the three chamber geometries (i.e., 60 times greater than a spherical point source) and therefore has the highest β_c/β_m, consistent with analytical results from Anderson and Segall (2011).

Here we quantify the effects of varying μ and the chamber geometry on $\bar{V}$ (Figures 6c and 6d). The $\bar{V}$ for crustal rocks with $\mu = 0.1$ GPa is up to a maximum of ~360% greater than that with $\mu = 2.1$ GPa at 2.5 km depth.

15252027, 2022, 7, Downloaded from https://agupubs.onlinelibrary.wiley.com/doi/10.1029/2022GC010387 by Alaska State Library, Wiley Online Library on [23/06/2025]. See the Terms and Conditions (https://onlinelibrary.wiley.com/terms-and-conditions) on Wiley Online Library for rules of use; OA articles are governed by the applicable Creative Commons License

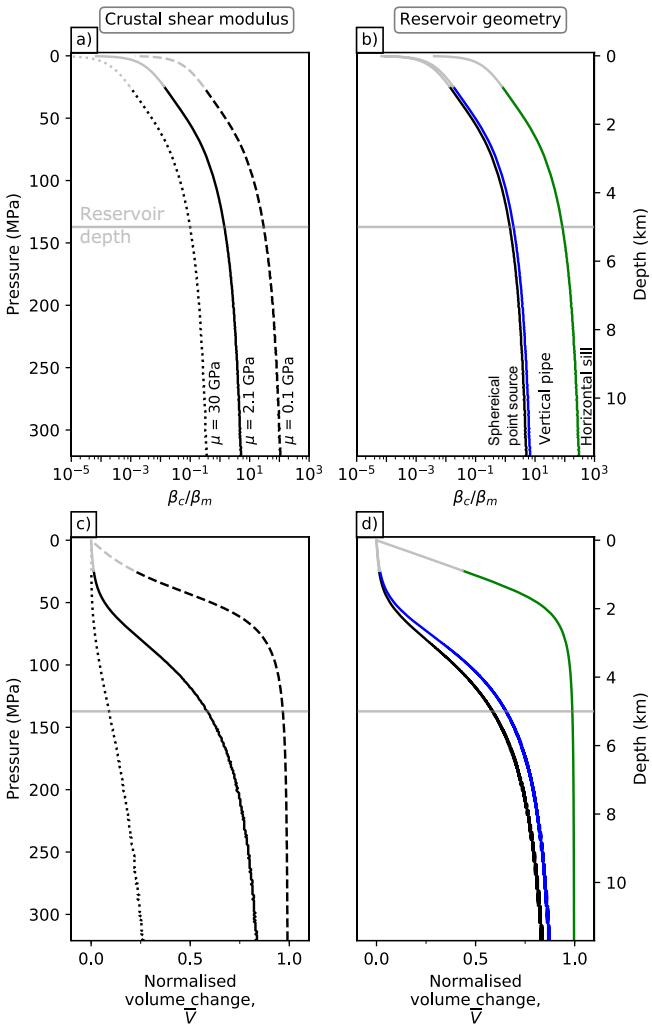

Figure 6. Physical properties of basalts when varying the crustal shear modulus (μ) and chamber geometry. (a) The ratio of β_c/β_m to illustrate the effects of crustal shear modulus and chamber geometry. The μ used are 0.1 GPa, 2.1 and 30 GPa (Heap et al., 2020), and the chamber geometry considered is of a spherical point source. (b) The ratio of β_c/β_m for a spherical point source, a vertical pipe-like chamber and a horizontal sill with $\mu = 2.1$ GPa. The major to minor semiaxis of the horizontal sill, $\frac{a}{c}$, is 100. (c) $\bar{V}$ for a spherical point source with varying μ. (d) $\bar{V}$ for a spherical point source, a vertical pipe-like chamber and a horizontal sill with $\mu = 2.1$ GPa. Fixed parameters: $w^{H_2O} = 2.0$ wt%, $w^{CO_2} = 3000$ ppm, $f_{O_2} =$ NNO, and $w^S = 2000$ ppm. The gray lines represent magma properties when percolation threshold exceeds $\phi_c = 37$ vol%.

In contrast, $\bar{V}$ is reduced up to a maximum of $\sim 73\%$ at 9.1 km depth for a crust with $\mu = 30$ GPa when compared to $\mu = 2.1$ GPa. At 5 km depth, the $\bar{V}$ for $\mu = 0.1$ GPa, 2.1 and 30 GPa are 0.97, 0.59 and 0.090, respectively (Figure 6c). The effects of different chamber geometries on $\bar{V}$ are shown in Figure 6d, with $\mu = 2.1$ GPa and Poisson's ratio ν of 0.30 (Heap et al., 2020). The normalized volume change $\bar{V}$ is greatest for horizontal sills and smallest for spherical point source, such that $\bar{V} = 0.99$ and 0.58, respectively, for a chamber at 5 km depth. Based on the effects of μ and chamber geometry on β_c/β_m, we find that a volcano with low β_c/β_m (i.e., spherical, high shear modulus) has low $\bar{V}$ which indicates muted volcanic deformation. In contrast, a volcano with high β_c/β_m (i.e., horizontal sill, low shear modulus) has high $\bar{V}$. For example, at 5 km depth, $\bar{V} = 0.090$ for a spherical point source with $\mu = 30$ GPa, but $\bar{V} = 1.0$ for a sill with $\mu = 0.1$ GPa.

The main takeaways from the sensitivity analysis of chamber compressibility is that 1) spherical point sources and vertical pipe-like chambers have similar β_c/β_m and $\bar{V}$, whereas sills have higher β_c/β_m and thus high $\bar{V}$ (Figures 2, 6b and 6d) crustal properties, specifically shear modulus, have a significant influence on $\bar{V}$, with lower crustal shear modulus contributing to larger volume changes (Figures 6a and 6c; Hautmann et al., 2010; Heap et al., 2020).

4.6. Summary of Sensitivity Analyses

Here we summarize the results from each sensitivity test. A summary of the greatest percentage change of $\bar{S}$, $\bar{V}$ and $\bar{z}$ over the depth range of each parameter is shown in Table 2. Our simplified model predicts that explosive eruptions of water-rich basaltic magmas have high SO_2 emissions and little deformation for a particular volume of magma erupted. While initial magmatic CO_2 causes insignificant changes to the total amount of SO_2 degassing during eruptions, it has significant impact on the observed co-eruptive deformation, that is, CO_2-rich magmas are more compressible than CO_2-poor magmas with the same amount of H_2O. Additionally, we find that varying magmatic CO_2 content from 1000 to 5000 ppm affects the observed co-eruptive deformation at a magnitude similar to that of varying initial magmatic H_2O content from 1.0 to 3.0 wt%, which implies that initial magmatic CO_2 content also plays an important role in magma compressibility and thus co-eruptive deformation. Initial magmatic S and oxygen fugacity have a strong influence on the magnitude of SO_2 degassing but have a minimal impact on the magnitude of the co-eruptive deformation. Magmas with a high oxygen fugacity yield high SO_2 emissions during an eruption, but this does not impact co-eruptive deformation significantly. Magmatic reservoirs with strong surrounding crustal rocks (i.e., high μ) and spherical geometry may display muted co-eruptive deformation when compared to compliant host rocks (i.e., low μ) and horizontal sills.

5. Comparison Between Arc Basalts and Ocean Island Basalts

5.1. Thermodynamic Modeling of Magma Properties

We now examine how tectonic setting influences the physicochemical properties of basaltic magma and consequently its impact on observed volcanic deformation and SO_2 degassing. Here we compare arc basalts and ocean island basalts by considering realistic parameter combinations and the co-dependence of parameters. Basaltic magma in arc settings tend to have higher water contents than basaltic magma from ocean island settings (e.g.,

15252027, 2022, 7, Downloaded from https://agupubs.onlinelibrary.wiley.com/doi/10.1029/2022GC010387 by Alaska State Library, Wiley Online Library on [23/06/2025]. See the Terms and Conditions (https://onlinelibrary.wiley.com/terms-and-conditions) on Wiley Online Library for rules of use; OA articles are governed by the applicable Creative Commons License

15252027, 2022, 7, Downloaded from https://agupubs.onlinelibrary.wiley.com/doi/10.1029/2022GC010387 by Alaska State Library, Wiley Online Library on [23/06/2025]. See the Terms and Conditions (https://onlinelibrary.wiley.com/terms-and-conditions) on Wiley Online Library for rules of use; OA articles are governed by the applicable Creative Commons License

Plank et al., 2013; Wallace, 2005; Zimmer et al., 2010). Melt inclusion data suggest that, on average, arc basalts contain 3.9 ± 0.4 wt% H_2O, 4000 ± 1000 ppm CO_2, and 3000 ± 1000 ppm S, and ocean island basalts contain 1.0 ± 0.2 wt% H_2O, 6500 ± 3500 ppm CO_2 and 1600 ± 1000 ppm S (e.g., Plank et al., 2013; Rasmussen et al., 2022; Ruscitto et al., 2012; Wallace, 2005). We note that the CO_2 content for ocean island basalts is at the high end of previous estimates and has high uncertainty, and this is because it was chosen to include CO_2-rich ocean island eruptions like Kīlauea (e.g., Dixon & Clague, 2001; Gerlach et al., 2002). These values represent the dissolved volatile abundances at shallow crustal levels, in which the volatiles recorded in the melt inclusions are primarily controlled by solubility. We take typical values of f_{O_2} of arc basalts and ocean island basalts at NNO + 1.4 ± 1 and NNO + 0.7 ± 0.9, respectively (e.g., Brounce et al., 2017; Konecke et al., 2019; Matjuschkin et al., 2016). Crustal compressibility also influences the magnitude of volcanic deformation (Section 4.5), and thus we use $\mu = 2.1$ GPa, which is typical in volcanic areas, and assume a Mogi deformation source for simplicity (A. Gudmundsson, 2005; Heap et al., 2020; Mogi, 1958). The range of parameter values used for the analyses described below are based on the magma composition typical for arc basalt and ocean island basalt (Table 1).

Monte-Carlo simulation allows repeated random sampling over a given input parameter space and hence allows us to estimate the possible range of model outputs. Here we use the range of magma compositions in typical arc and ocean island basalts to estimate the ranges of volume change, ground deformation and SO_2 flux expected for eruptions in different tectonic settings. We performed 1000 simulations for each type using the distribution of each variable (w^{H_2O}, w^{CO_2}, w^S, f_{O_2}) provided in Table 1 as input parameters for the thermodynamic model. Parameters that are distributed below the detection limit are readjusted accordingly (i.e., $w^{H_2O} < 100$ ppm, $w^{CO_2} < 25$ ppm and $w^S < 50$ ppm are changed to $w^{H_2O} = 100$ ppm, $w^{CO_2} = 25$ ppm and $w^S = 50$ ppm, respectively). The thermodynamic model has a starting temperature of 1200°C, a Poisson's ratio v of 0.30, and we find the starting pressure/depth using the saturation point of each melt composition. After 1000 Monte Carlo simulations, we calculate the mean and the standard deviation for each model output, such as normalized SO_2, magma compressibility and normalized volume change. Since we started each simulation at the saturation point for that composition (see Section 3.1), we apply a filter to discard the values for any pressure/depth with less than 100 successful simulations.

In Figure 7 we present the model predictions for arc basalts and ocean island basalts to illustrate the effects of tectonic settings on magma properties and co-eruptive observations. The high f_{O_2} environment of arc basalts will tend to produce more exsolved SO_2 at the expense of H_2S and S_2, whereas ocean island basalts, which have a lower f_{O_2}, have less exsolved SO_2 in the gas phase (Figure 7b). With a higher mole fraction of exsolved SO_2 gas, the predicted $\bar{S}$ (i.e., SO_2 gas in the reservoir) of arc basalts is higher than that of ocean island basalts (Figure 7c). In contrast, for basaltic eruptions that undergo co-eruptive degassing, such that additional sulfur is loss from melt during the final ascent to the surface, the difference in $\bar{S}$ would be expected to result from differences in initial magmatic sulfur content and f_{O_2}. The higher magmatic volatile content of arc basalts translates to a higher V_g (Figure 7d), suggesting that in general, arc basalts are more compressible than ocean island basalts (Figure 7f). We note that while our study uses a higher CO_2 content for ocean island basalts than arc basalts (Table 1), water-rich arc basalts remain more compressible than ocean island basalts, which highlights that the range of H_2O content in basalts plays a more important role in determining magma compressibility than CO_2 content. The increased magma compressibility indicates that arc basalts have a lower $\bar{V}$ and $\bar{z}$ than ocean island basalts (Figures 7g and 7h).

Here we give specific values for arc basalts and ocean island basalts assuming a magma chamber at 5 km depth (Figure 7). If an explosive eruption should occur from a chamber at 5 km depth (where we assume that volatiles are in both exsolved and dissolved form in the magma chamber and that no co-eruptive degassing occurs during magma ascent), the predicted $\bar{S}$ of arc basalts is 0.60 kg m^{-3}, greater than that of ocean island basalts at 0.14 kg m^{-3} (Figure 7c). For a chamber at 5 km depth, arc basalts are more compressible than ocean island basalts at $\beta_m = 12 \times 10^{-10}$ Pa^{-1} and 3.3×10^{-10} Pa^{-1}, respectively (Figure 7f), and thus arc basalts have $\bar{V} = 0.24$ and $\bar{z} = 2.3$ m km^{-3} as compared to ocean island basalts that have $\bar{V} = 0.52$ and $\bar{z} = 5.0$ m km^{-3}. It is noted that ocean island basalts eruptions are usually effusive in nature (i.e., they will exhibit extensive co-eruptive degassing; see Section 2), and thus we expect $\bar{S}$ to be dominated by decompressional degassing and hence much higher than predicted the gas content in the chamber.

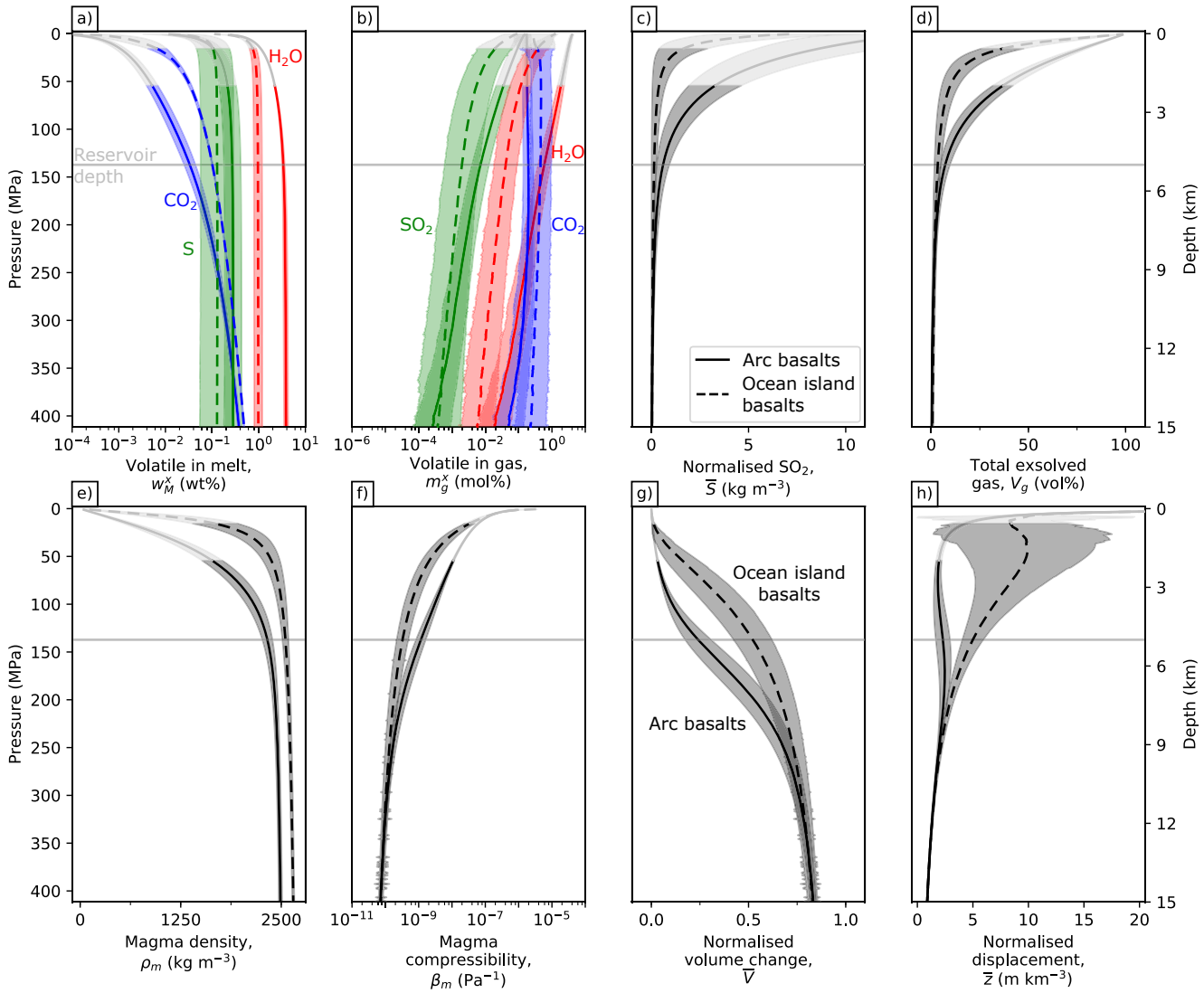

Figure 7. Comparison of magma properties between typical arc basalts (full line) and typical ocean island basalts (dashed line). The input parameters for the thermodynamic model (w^{H_2O}, w^{CO_2} w^S and f_{O_2}) and crustal shear modulus μ are initialized using a Monte-Carlo approach (Table 1). 1000 simulations are performed and the magma properties are calculated using the thermodynamic framework. (a) Weight fraction of dissolved volatile contents and (b) mol fraction of exsolved volatile contents. (c) Normalized SO_2 $\bar{S}$. (d) Volume fraction of exsolved gases in magma (V_g). (e) Magma density (ρ_m) and (f) Magma compressibility (β_m). (g) Normalized volume change $(\bar{V})$. (h) Normalized vertical displacement ($\bar{z}$). The gray lines represent magma properties after exceeding percolation threshold $\phi_c = 37$ vol% and the shaded region represent 1σ uncertainty. The range of parameter values for arc basalts and ocean island basalts are listed in Table 1.

5.2. Comparison to Satellite Observations

In this section, we compare the magma properties predicted by the thermodynamic framework with observations of eruptions to understand published catalogs of volcanic deformation and degassing.

5.2.1. Data Compilation

Here we compiled deformation and SO_2 degassing data for 94 basaltic eruptions during the satellite era (2005–2020) to understand how theoretical estimates from thermodynamic modeling compare with observed eruptions (Table S1 in Supporting Information S1). The primary magma composition and the dates for past eruptions are drawn from the Global Volcanism Program (2013). The compilation only considers volcanoes of basaltic composition. For eruptions with poorly constrained starting or ending dates, particularly for long-lived eruptions, we select the dates at which significant eruptions occur such as the the 2018 eruptions of Kīlauea, Ambrym and Fuego (e.g., Hamling et al., 2019; Naismith et al., 2019; Neal et al., 2019).

15252027, 2022, 7, Downloaded from https://agupubs.onlinelibrary.wiley.com/doi/10.1029/2022GC010387 by Alaska State Library, Wiley Online Library on [23/06/2025]. See the Terms and Conditions (https://onlinelibrary.wiley.com/terms-and-conditions) on Wiley Online Library for rules of use; OA articles are governed by the applicable Creative Commons License

15252027, 2022, 7, Downloaded from https://agupubs.onlinelibrary.wiley.com/doi/10.1029/2022GC010387 by Alaska State Library, Wiley Online Library on [23/06/2025]. See the Terms and Conditions (https://onlinelibrary.wiley.com/terms-and-conditions) on Wiley Online Library for rules of use; OA articles are governed by the applicable Creative Commons License

We compile 23 episodes of pre- and co-eruptive deformation detected with InSAR from the published catalogs of Biggs and Pritchard (2017) and Ebmeier et al. (2018) and 58 satellite observations of SO_2 degassing from individual studies (Data Set S1), published catalogs (Carn et al., 2016, 2017) and Global Volcanism Program (2013). For eruptions that are less well studied (e.g., Chikurachki, Pagan, Semisopochnoi), evidence for SO_2 degassing are crosschecked with the Global Sulfur Dioxide Monitoring homepage (https://so2.gsfc.nasa.gov/). Persistently degassing volcanoes (e.g., Shishaldin, Saunders, Korovin), including those whose emissions can be detected by satellites (e.g., Masaya, Miyakejima, Telica) (Carn et al., 2017), and submarine eruptions (e.g., Mayotte, Axial Seamount, Bristol Island) are not considered in this compilation. We also do not consider volcanoes that have approximately equal passive and eruptive SO_2 degassing such as Rabaul (Carn et al., 2016), with the exception of VEI 4+ eruptions (e.g., the 2005 and 2014 eruption of Manam and the 2019 eruption of Ulawun). We do, however, include eruptions that are significantly explosive (e.g., 2018 eruptions of Ambrym and Kīlauea).

We find that observations of deformation and SO_2 degassing are not available for every eruption despite similar erupted volume or volcano (Figure 8b). In fact, there is no clear correlation between satellite observations and erupted volume, consistent with previous studies (Kilbride et al., 2016), largely due to the challenges in volcano monitoring such as atmospheric noise, ice cover, or limitations in satellite sensors (e.g., Ozone Monitoring Instrument (OMI) row anomaly for the 2012 eruption of Tolbachik). For example, satellite sensors could not measure the deformation associated with the 2011 eruption of Grimsvötn due to ice cover. Similarly, satellite measurement of SO_2 degassing is not available for the 2012–2013 eruption of Tolbachik, despite being one of the most voluminous arc basalt eruptions (Belousov et al., 2015), due to the OMI row anomaly (see https://so2.gsfc.nasa.gov/pix/daily/1112/kamchat_1112z.html).

Overall, deformation was detected at 25% of eruptions (23/94) and SO_2 degassing at 62% of eruptions (58/94) (Table S1 in Supporting Information S1). A similar analysis conducted by Furtney et al. (2018) uses multiple satellite data spanning 1978–2016 to synthesize observations of volcanic deformation and degassing. Their study yielded similar results to ours: of the 250 volcanic eruptions between 1978 and 2016, 28% of eruptions have satellite observations of volcanic deformation, and SO_2 degassing is observed at 67% of eruptions (Furtney et al., 2018). We note that the Furtney et al. (2018) study includes a wider range of magma composition than we do here, so the slightly higher proportion of volcanoes with satellite-detected deformation and degassing analyzed by Furtney et al. (2018) is likely caused by the inclusion of magma of varying compositions and also pre- and post-eruptive observations. The overall proportion of satellite observations of volcanic deformation and SO_2 degassing appears to be fairly consistent between studies.

5.2.2. Comparison Between Tectonic Settings

Our compilation shows that co-eruptive deformation has been observed at 48% of eruptions involving ocean island basalts (16/33), while only 11% of arc basalt eruptions had observed deformation (7/61) (Figure 8a). The lower frequency of detectable deformation at arc basalt eruptions can be attributed to the higher volatile contents of arc magmas, which our thermodynamic model predicts will increase magma compressibility and reduce surface deformation (Figures 7f–7h). Systematic satellite observations of deformation spanning 1992–2010 analyzed by Biggs, Ebmeier, et al. (2014) shows that the proportion of deforming volcanoes that erupted is higher for volcanoes in hotspot setting (66%; ocean island) as compared to those in subduction setting (53%; arc). For example, there are few InSAR observations from the Central American Volcanic Arc, where parental melts are water-rich (Ebmeier et al., 2013a; Wallace, 2005). Although this is an indirect comparison, the study agrees well with our results that observations of volcanic deformation are dominated by ocean island basalt eruptions. However, we note that other potential factors may also contribute to the lack of detectable deformation at volcanoes, independently or collectively (e.g., the rate of magma recharge, chamber geometry, depth of magma storage, viscoelastic crustal rheology, an open conduit, pre-eruptive degassing, atmospheric noise (Chaussard et al., 2013; Ebmeier et al., 2013a, 2013b; Head et al., 2019; Mullet & Segall, 2022; Yip et al., 2019)) meaning that the models are very uncertain.

Volcanic SO_2 degassing was observed at all 33 ocean island basalt eruptions in our compilation but at only 41% of the arc basalt eruptions (25/61) (Data Set S1; Figure 8a). While the higher magmatic volatile content of arc basalts might be expected to produce a higher detection rate (Figure 7c), the high rate of detection at ocean island basalt can be attributed to co-eruptive degassing during effusive eruptions. Conversely, the explosive nature of arc basalt eruptions may mean there is no co-eruptive degassing and the only volatiles released are those in equilibrium at chamber depth. Additionally, technical difficulties in spectrometers, such as the OMI row anomaly that

10.1029/2022GC010387

a)

	Arc basalt	Ocean island basalt
Eruptions (2005–2020)	61	33
Satellite-detected deformation	7	16
Satellite-detected SO_2 degassing	25	33
Satellite-detected SO_2 degassing and deformation	4	16
Absence of satellite-detected SO_2 degassing and deformation	3	0

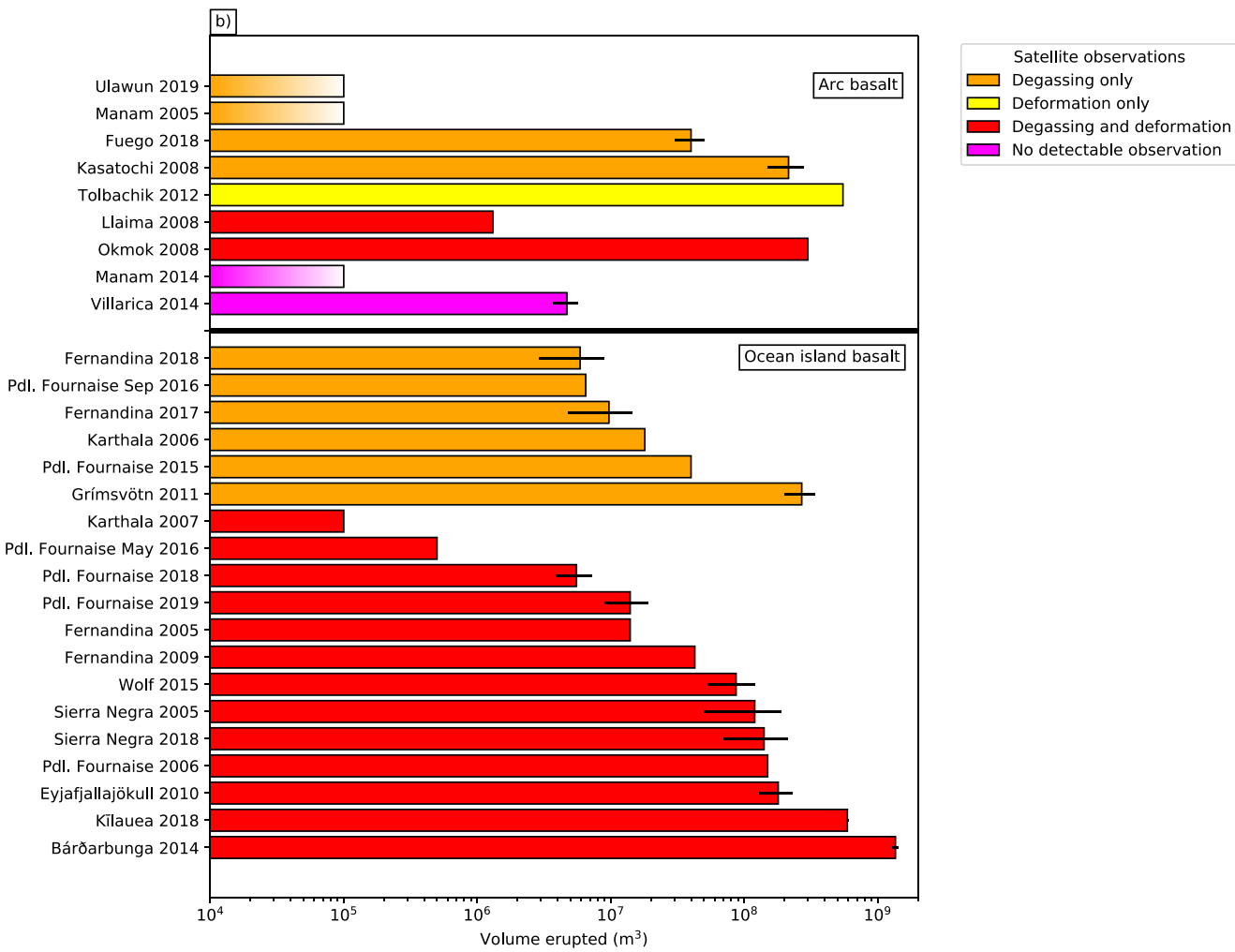

Figure 8. (a) Number of arc basalt and ocean island basalt eruptions with volcanic deformation (either uplift or subsidence) and SO_2 degassing measured by satellites during the satellite era (2005–2020). (b) Arc basalt and ocean island basalt eruptions with erupted volume greater than 10^5 m^3. Columns are color-coded for deformation and SO_2 degassing detectable by satellites. Uncertainties in the erupted volume, where available, are shown as horizontal error bars. Eruptions with a color gradient use VEI index as a very rough indicator to estimate the erupted volume. We assume VEI 4 eruptions to have a volume > 10^5 m^3.

15252027, 2022, 7, Downloaded from https://agupubs.onlinelibrary.wiley.com/doi/10.1029/2022GC010387 by Alaska State Library, Wiley Online Library on [23/06/2025]. See the Terms and Conditions (https://onlinelibrary.wiley.com/terms-and-conditions) on Wiley Online Library for rules of use; OA articles are governed by the applicable Creative Commons License

obscures the spectrometer's field of view (e.g., 2019 eruption of Klyuchevskoy, 2012 eruption of Tolbachik; see https://so2.gsfc.nasa.gov/) prevents routine volcano monitoring.

We find that satellite observations of both volcanic deformation and degassing to be higher for ocean island basalt eruptions (16/33) than arc basalt eruptions (4/61) (Figure 8a). We note that despite the much higher number of arc eruptions in our catalog than ocean island eruptions, there are very much fewer observations of deformation for arc eruptions. Similarly, all ocean island basalt eruptions have been observed by at least one satellite sensor, while 3 of the 61 arc basalt eruptions were not detected by either sensors. The lack of satellite observations of arc basalt eruptions highlights the difficulties in monitoring explosive eruptions with high magmatic volatile contents and thus compressible magmas (Huppert & Woods, 2002; Kilbride et al., 2016; Rivalta & Segall, 2008), and volcanoes with deep magma storage prior to eruptions (Ebmeier et al., 2013a; Moran et al., 2006).

Finally, we further analyze 28 eruptions with erupted volume $\geq 10^5$ m^3 (Figure 8b) to ensure comparable detection thresholds (Table S2 in Supporting Information S1). We note that there is a lack of data on the erupted volume, which may result in sampling bias and therefore, we extend our search using the VEI index drawn from the Global Volcanism Program (2013) with the assumption that VEI 4 eruptions produce $\geq 10^5$ m^3 DRE and that they are significantly explosive. All 19 ocean island basalt eruptions with erupted volume $\geq 10^5$ m^3 have satellite observations of SO_2 degassing of which 13 have deformation measured by satellites (Figure 8b). For the case of arc basalt eruptions, there are only 9 instances of eruptions with $\geq 10^5$ m^3 DRE, of which 3 are estimated from the VEI index (the 2005 and 2014 eruption of Manam and the 2019 eruption of Ulawun) (Figure 8b). We find that one arc eruption has satellite observation of co-eruptive deformation, four have satellite observations of SO_2 degassing and two have observations of both deformation and degassing. The two remaining eruptions, the 2014 eruption of Manam and Villarica, were not detected by satellites, probably due to atmospheric noise (lack of co-eruptive deformation at Villarica, Delgado et al., 2017) and OMI row anomaly (see https://so2.gsfc.nasa.gov/). As such, we find no link between erupted volume $\geq 10^5$ m^3 and satellite observations of SO_2 degassing and deformation (Figure 8b), in agreement with the wider catalog and previous studies (Kilbride et al., 2016). This highlights the challenges for satellites to detect surface deformation, particularly for eruptions of more evolved, volatile-rich arc magmas that are more compressible.

In summary, the thermodynamic framework and satellite observations of deformation agree well with each other such that volcanic deformation of volatile-poor ocean island eruptions are more likely to be detected by satellites as compared to volatile-rich arc eruptions (Figures 7g and 7h; Figure 8a). This is because volatile-rich arc basalts are highly compressible, which results in muted surface deformation. Predictions of SO_2 degassing from our thermodynamic framework show that volatile-rich arc basalts have higher rates of SO_2 degassing at chamber depths, yet satellite observations show that ocean island eruptions outgas more SO_2 per unit of magma erupted (Figure 7c; Figure 8a), due to extensive co-eruptive degassing. We note that while the water content of arc basalts is two times greater than that of ocean island basalts, the sulfur content in basalts from both tectonic settings are similar (Table 1).

6. Limitations of Our Model

The high magmatic volatile contents of arc basalts, and their oxidized nature, lead to a substantial amount of exsolved volatiles being present in the chamber prior to eruption, which increases magma compressibility and lessens the magnitude of volcanic deformation (Figure 7). Co-eruptive deformation is less likely to be detected at arc volcanoes than at volcanoes in ocean island settings (Figure 8). However, we note that the high initial volatile content of a magma body is not the only factor that affects the magnitude of volcanic deformation. Other potential factors include (a) magma chambers with different geometries (e.g., A. Gudmundsson, 2008; Amoruso & Crescentini, 2009; Anderson & Segall, 2011), (b) the influence of the viscoelastic response of the crust (e.g., Gottsmann et al., 2020; Head et al., 2019; Hickey et al., 2013), and (c) the presence of a "transcrustal" mush surrounding the magma body (e.g., Cashman et al., 2017; Sparks et al., 2019). It has been shown that the magnitude of the syn-eruptive surface deformation signal for a volcano overlying a transcrustal mush system would be less than that with a simple magma body in a rigid sub-solidus country rock, and this effect increases with the melt fraction of the mush (Mullet & Segall, 2022). Estimates of magma compressibility and the volume change of a magma reservoir are likely to be underestimated assuming the magma body is contained within an elastic half space rather than a mush-like system (Mullet & Segall, 2022).

15252027, 2022, 7, Downloaded from https://agupubs.onlinelibrary.wiley.com/doi/10.1029/2022GC010387 by Alaska State Library, Wiley Online Library on [23/06/2025]. See the Terms and Conditions (https://onlinelibrary.wiley.com/terms-and-conditions) on Wiley Online Library for rules of use; OA articles are governed by the applicable Creative Commons License

15252027, 2022, 7, Downloaded from https://agupubs.onlinelibrary.wiley.com/doi/10.1029/2022GC010387 by Alaska State Library, Wiley Online Library on [23/06/2025]. See the Terms and Conditions (https://onlinelibrary.wiley.com/terms-and-conditions) on Wiley Online Library for rules of use; OA articles are governed by the applicable Creative Commons License

Our model also predicts that explosive eruptions of arc basalts will produce a higher syn-eruptive SO_2 flux than ocean island basalt eruptions. However, sulfur in basaltic magma has a high diffusivity and can continue to exsolve extensively during magma ascent, particularly during effusive eruptions (Figure 1c). Differences between the predicted SO_2 gas per unit volume of magma in the chamber and that observed during an eruption may be modified by (a) co-eruptive degassing, (b) epistemic uncertainties in model parameters associated with initial magmatic sulfur content and f_{O_2}, (c) pre-eruptive gas accumulation and loss (e.g., Edmonds et al., 2014; Edmonds & Woods, 2018; Wallace, 2005), (d) sulfur loss due to scrubbing or formation of sulfide globules (e.g., Anderson & Poland, 2016; Hurwitz & Anderson, 2019; Sigmarsson et al., 2013). Furthermore, we note that the solubility of sulfur species are calculated using a sulfide capacity law that is more appropriate for sulfur in reduced melt (O'Neill, 2021; Liggins et al., 2020, 2021).

The simplicity of this model is useful for considering general trends, and we note that oversimplification reduces the applicability to individual eruptions. The assumption of a typical elastic shear modulus may be appropriate for the sensitivity tests, but crustal rheology varies enormously between volcanoes (e.g., A. Gudmundsson, 2005; Head et al., 2019; Heap et al., 2020; Huber et al., 2019). We also consider that only depth (i.e., pressure) affects the amount of exsolved gas content in bulk magma for a given set of initial conditions, such that the magma does not undergo crystallisation nor magma recharge, which is very simplistic. Additionally, we did not consider the effects of pre-eruptive gas accumulation and loss on magma properties, which in reality could affect co-eruptive observations (e.g., Huppert & Woods, 2002; Rivalta & Segall, 2008; Wallace, 2001). While simplistic, our principal findings remains robust and we highlight the importance of exsolved magmatic H_2O in controlling magma compressibility, which helps to explain the lack of volcanic deformation that accompanies many arc eruptions.

7. Conclusion

The thermodynamic framework presented in this study provides a quantitative link between observations of volcanic deformation and degassing. The framework is used to explore the sensitivity of magma properties to several controlling parameters (magmatic H_2O, magmatic CO_2, magmatic S, oxygen fugacity f_{O_2}), which vary systematically between tectonic setting. We demonstrated that the results from thermodynamic models can be used to calculate the volume of gas in the reservoir, which can be related to SO_2 emissions and surface deformation. The conclusions of this study are as follows:

1. Magmas with a high magmatic H_2O content have high volumes of exsolved gas in the chamber, leading to high magma compressibility, which results in muted surface deformation during eruptions. While high magmatic CO_2 has little effect on SO_2 degassing, it increases magma compressibility and thus reduces surface deformation. Varying oxygen fugacity from NNO−1 to NNO+2 and increasing magmatic S contents increases SO_2 gas emissions but has little effect on magma compressibility.
2. The volatile content of magmas varies between tectonic settings and this influences both ground deformation and the extent of degassing during eruptions. Arc basalts, which tend to have higher magmatic volatile contents, have more muted ground deformation than ocean island basalts, which is reflected in observations over the satellite era.

With results from the thermodynamic framework, we have developed a better understanding of the effects of magmatic volatile content and degassing on the physicochemical properties of magma. Our future work will explore pre-eruptive gas segregation processes such as gas accumulation and percolative gas loss to understand their implications for observations of volcanic deformation and degassing. Future studies should refine this framework for specific circumstances to resolve additional complexities.

Data Availability Statement

The EVo thermodynamic model used here, the data generated in this study and the Jupyter Notebook associated with the thermodynamic framework has been archived on Zenodo (https://doi.org/10.5281/zenodo.6628504).

Acknowledgments
This research is supported by the NERC-BGS Centre for the Observation and Modelling of Earthquakes Volcanoes and Tectonics (COMET) for SY, JB and ME. SY and JB are funded by the Leverhulme Trust, and PL acknowledges funding from the Embiricos Trust Scholarship from Jesus College, Cambridge. The authors would like to thank Paul Wallace and an anonymous reviewer, along with Editor Paul Asimow for their very constructive and detailed feedback that greatly improve this manuscript.

References

Albino, F., Biggs, J., & Syahbana, D. K. (2019). Dyke intrusion between neighbouring arc volcanoes re-sponsible for 2017 pre-eruptive seismic swarm at Agung, Bali. *Nature Communications*, *10*(1), 748. https://doi.org/10.1038/s41467-019-08564-9

Amoruso, A., & Crescentini, L. (2009). Shape and volume change of pressurized ellipsoidal cavities from deformation and seismic data. *Journal of Geophysical Research*, *114*(B2), B02210. https://doi.org/10.1029/2008jb005946

Anderson, K., & Poland, M. P. (2016). Bayesian estimation of magma supply, storage, and eruption rates using a multiphysical volcano model: Kīlauea Volcano, 2000–2012. *Earth and Planetary Science Letters*, *447*, 161–171. https://doi.org/10.1016/j.epsl.2016.04.029

Anderson, K., & Segall, P. (2011). Physics-based models of ground deformation and extrusion rate at effusively erupting volcanoes. *Journal of Geophysical Research*, *116*(7), 1–20. https://doi.org/10.1029/2010jb007939

Avouris, D. M., Carn, S. A., & Waite, G. P. (2017). Triggering of volcanic degassing by large earthquakes. *Geology*, *45*(8), 715–718. https://doi.org/10.1130/g39074.1

Bachmann, O., & Bergantz, G. W. (2006). Gas percolation in upper-crustal silicic crystal mushes as a mechanism for upward heat advection and rejuvenation of near-solidus magma bodies. *Journal of Volcanology and Geothermal Research*, *149*(1–2), 85–102. https://doi.org/10.1016/J.JVOLGEORES.2005.06.002

Belousov, A., Belousova, M., Edwards, B., Volynets, A., & Melnikov, D. (2015). Overview of the precursors and dynamics of the 2012-13 basaltic fissure eruption of Tolbachik Volcano, Kamchatka, Russia. *Journal of Volcanology and Geothermal Research*, *307*, 22–37. https://doi.org/10.1016/j.jvolgeores.2015.06.013

Biggs, J., Ebmeier, S. K., Aspinall, W. P., Lu, Z., Pritchard, M. E., Sparks, R. S., & Mather, T. A. (2014). Global link between deformation and volcanic eruption quantified by satellite imagery. *Nature Communications*, *5*. https://doi.org/10.1038/ncomms4471

Biggs, J., & Pritchard, M. E. (2017). Global volcano monitoring: What does it mean when volcanoes deform? *Elements*, *13*(1), 17–22. https://doi.org/10.2113/gselements.13.1.17

Biggs, J., & Wright, T. J. (2020). How satellite InSAR has grown from opportunistic science to routine monitoring over the last decade. *Nature Research*, *11* (1). https://doi.org/10.1038/s41467-020-17587-6

Brounce, M., Stolper, E., & Eiler, J. (2017). Redox variations in Mauna Kea lavas, the oxygen fugacity of the Hawaiian plume, and the role of volcanic gases in Earth's oxygenation. *Proceedings of the National Academy of Sciences of the United States of America*, *114*(34), 8997–9002. https://doi.org/10.1073/pnas.1619527114

Burgisser, A., Alletti, M., & Scaillet, B. (2015). Simulating the behavior of volatiles belonging to the C-O-H-S system in silicate melts under magmatic conditions with the software D-Compress. *Computers & Geosciences*, *79*, 1–14. https://doi.org/10.1016/j.cageo.2015.03.002

Burgisser, A., Chevalier, L., Gardner, J. E., & Castro, J. M. (2017). The percolation threshold and permeability evolution of ascending magmas. *Earth and Planetary Science Letters*, *470*, 37–47. https://doi.org/10.1016/j.epsl.2017.04.023

Candela, P. (1997). A review of shallow, ore-related granites: Textures, volatiles, and ore metals. *Journal of Petrology*, *38*(12), 1619–1633. https://doi.org/10.1093/petroj/38.12.1619

Candela, P., & Piccoli, P. (1998). Magmatic contributions to hydrothermal ore deposits: An algorithm (MVPart) for calculating the composition of the magmatic volatile phase. *Techniques in Hydrothermal Ore Deposits Geology*. https://doi.org/10.5382/REV.10.04

Carboni, E., Grainger, R. G., Mather, T. A., Pyle, D. M., Thomas, G. E., Siddans, R., et al. (2016). The vertical distribution of volcanic SO2 plumes measured by IASI. *Atmospheric Chemistry and Physics*, *16*(7), 4343–4367. https://doi.org/10.5194/acp-16-4343-2016

Carn, S. A., Clarisse, L., & Prata, A. J. (2016). Multi-decadal satellite measurements of global volcanic degassing. *Journal of Volcanology and Geothermal Research*, *311*, 99–134. https://doi.org/10.1016/j.jvolgeores.2016.01.002

Carn, S. A., Fioletov, V. E., Mclinden, C. A., Li, C., & Krotkov, N. A. (2017). A decade of global volcanic SO2 emissions measured from space. *Scientific Reports*, *7*(1), 1–12. https://doi.org/10.1038/srep44095

Cashman, K. V., Sparks, R. S. J., & Blundy, J. D. (2017). Vertically extensive and unstable magmatic systems: A unified view of igneous processes. *Science*, *355*(6331). https://doi.org/10.1126/science.aag3055

Chaussard, E., & Amelung, F. (2014). Regional controls on magma ascent and storage in volcanic arcs. *Geochemistry, Geophysics, Geosystems*, *15*(4), 1407–1418. https://doi.org/10.1002/2013gc005216

Chaussard, E., Amelung, F., & Aoki, Y. (2013). Characterization of open and closed volcanic systems in Indonesia and Mexico using InSAR time series. *Journal of Geophysical Research: Solid Earth*, *118*, 3957–3969. https://doi.org/10.1002/jgrb.50288

Collins, S. J., Pyle, D. M., & Maclennan, J. (2009). Melt inclusions track pre-eruption storage and dehydration of magmas at Etna. *Geology*, *37*(6), 571–574. https://doi.org/10.1130/G30040A.1

Colombier, M., Wadsworth, F. B., Scheu, B., Vasseur, J., Dobson, K. J., Cáceres, F., et al. (2020). In situ observation of the percolation threshold in multiphase magma analogues. *Bulletin of Volcanology*, *82*(4), 1–15. https://doi.org/10.1007/s00445-020-1370-1

Conde, V., Bredemeyer, S., Saballos, J. A., Galle, B., & Hansteen, T. H. (2015). Linking SO_2 emission rates and seismicity by continuous wavelet transform: Implications for volcanic surveillance at san cristóbal volcano, Nicaragua. *International Journal of Earth Sciences*, *105*(5), 1453–1465. https://doi.org/10.1007/S00531-015-1264-1

Coppola, D., Laiolo, M., Cigolini, C., Massimetti, F., Delle Donne, D., Ripepe, M., et al. (2020). Thermal remote sensing for global volcano monitoring: Experiences from the MIROVA system. *Frontiers of Earth Science*, *7*, 362. https://doi.org/10.3389/FEART.2019.00362/BIBTEX

Delgado, F., Pritchard, M. E., Ebmeier, S., González, P., & Lara, L. (2017). Recent unrest (2002–2015) imaged by space geodesy at the highest risk Chilean volcanoes: Villarrica, Llaima, and Calbuco (Southern Andes). *Journal of Volcanology and Geothermal Research*, *344*, 270–288. https://doi.org/10.1016/j.jvolgeores.2017.05.020

Dieterich, J. H., & Decker, R. W. (1975). Finite element modeling of surface deformation associated with volcanism. *Journal of Geophysical Research*, *80*(29), 4094–4102. https://doi.org/10.1029/JB080I029P04094

Dixon, J. E., & Clague, D. A. (2001). Volatiles in basaltic glasses from Loihi Seamount, Hawaii: Evidence for a relatively dry plume component. *Journal of Petrology*, *42*(3), 627–654. https://doi.org/10.1093/petrology/42.3.627

Duan, X. (2014). A general model for predicting the solubility behavior of H_2O-CO_2 fluids in silicate melts over a wide range of pressure, temperature and compositions. *Geochimica et Cosmochimica Acta*, *125*, 582–609. https://doi.org/10.1016/j.gca.2013.10.018

Ebmeier, S. K., Andrews, B. J., Araya, M. C., Arnold, D. W. D., Biggs, J., Cooper, C., et al. (2018). Synthesis of global satellite observations of magmatic and volcanic deformation: Implications for volcano monitoring & the lateral extent of magmatic domains. *Journal of Applied Volcanology*, *7*(1), 1–26. https://doi.org/10.1186/s13617-018-0071-3

Ebmeier, S. K., Biggs, J., Mather, T. A., & Amelung, F. (2013a). On the lack of InSAR observations of magmatic deformation at Central American volcanoes. *Journal of Geophysical Research: Solid Earth*, *118*(5), 2571–2585. https://doi.org/10.1002/jgrb.50195

Ebmeier, S. K., Biggs, J., Mather, T. A., & Amelung, F. (2013b). Applicability of InSAR to tropical volcanoes: Insights from central America. *Geological Society, London, Special Publications*, *380*, 15–37. https://doi.org/10.1144/SP380.2

15252027, 2022, 7, Downloaded from https://agupubs.onlinelibrary.wiley.com/doi/10.1029/2022GC010387 by Alaska State Library, Wiley Online Library on [23/06/2025]. See the Terms and Conditions (https://onlinelibrary.wiley.com/terms-and-conditions) on Wiley Online Library for rules of use; OA articles are governed by the applicable Creative Commons License

Ebmeier, S. K., Elliott, J. R., Nocquet, J. M., Biggs, J., Mothes, P., Jarrín, P., et al. (2016). Shallow earthquake inhibits unrest near Chiles–Cerro Negro volcanoes, Ecuador–Colombian border. *Earth and Planetary Science Letters*, *450*, 283–291. https://doi.org/10.1016/j.epsl.2016.06.046

Edmonds, M., Cashman, K. V., Holness, M., & Jackson, M. (2019). Architecture and dynamics of magma reservoirs. *Philosophical Transactions of the Royal Society A: Mathematical, Physical & Engineering Sciences*, *377*(2139), 20180298. https://doi.org/10.1098/rsta.2018.0298

Edmonds, M., Humphreys, M. C., Hauri, E. H., Herd, R. A., Wadge, G., Rawson, H., et al. (2014). Pre-eruptive vapour and its role in controlling eruption style and longevity at Soufrière Hills Volcano. *Geological Society Memoir*, *39*(1), 291–315. https://doi.org/10.1144/M39.16

Edmonds, M., Mather, T. A., & Liu, E. J. (2018). A distinct metal fingerprint in arc volcanic emissions. *Nature Geoscience*, *11*(10), 790–794. https://doi.org/10.1038/s41561-018-0214-5

Edmonds, M., & Woods, A. W. (2018). Exsolved volatiles in magma reservoirs. *Journal of Volcanology and Geothermal Research*, *368*, 13–30. https://doi.org/10.1016/j.jvolgeores.2018.10.018

Fialko, Y., Simons, M., & Agnew, D. (2001). The complete (3-D) surface displacement field in the epicentral area of the 1999 Mw 7.1 Hector Mine earthquake, California, from space geodetic observations. *Geophysical Research Letters*, *28*(16), 3063–3066. https://doi.org/10.1029/2001GL013174

Furtney, M. A., Pritchard, M. E., Biggs, J., Carn, S. A., Ebmeier, S. K., Jay, J. A., et al. (2018). Synthesizing multi-sensor, multi-satellite, multi-decadal datasets for global volcano monitoring. *Journal of Volcanology and Geothermal Research*, *365*, 38–56. https://doi.org/10.1016/j.jvolgeores.2018.10.002

Gaillard, F., & Scaillet, B. (2014). A theoretical framework for volcanic degassing chemistry in a comparative planetology perspective and implications for planetary atmospheres. *Earth and Planetary Science Letters*, *403*, 307–316. https://doi.org/10.1016/j.epsl.2014.07.009

Ge, C., Wang, J., Carn, S., Yang, K., Ginoux, P., & Krotkov, N. (2016). Satellite-based global volcanic SO2 emissions and sulfate direct radiative forcing during 2005-2012. *Journal of Geophysical Research*, *121*(7), 3446–3464. https://doi.org/10.1002/2015JD023134

Gerlach, T. M., Mcgee, K. A., Elias, T., Sutton, A. J., Doukas, M. P., Mcgee, T. A., et al. (2002). Carbon dioxide emission rate of Kīlauea Volcano: Implications for primary magma and the summit reservoir. *Journal of Geophysical Research*, *107*(B9), 1–3. https://doi.org/10.1029/2001JB000407

Girona, T., Costa, F., Newhall, C., & Taisne, B. (2014). On depressurization of volcanic magma reservoirs by passive degassing. *Journal of Geophysical Research: Solid Earth*, *119*(12), 8667–8687. https://doi.org/10.1002/2014jb011368

Global Volcanism Program. (2013). Volcanoes of the World (Version 4.9.2). In E. Venzke (ed.), Smithsonian Institution. https://doi.org/10.5479/si.GVP.VOTW4-2013

Gong, W., Meyer, F. J., Lee, C.-W., Lu, Z., & Freymueller, J. (2015). Measurement and interpretation of subtle deformation signals at Unimak Island from 2003 to 2010 using weather model-assisted time series InSAR. *Journal of Geophysical Research: Solid Earth*, *120*(2), 1175–1194. https://doi.org/10.1002/2014JB011384

Gottsmann, J., Biggs, J., Lloyd, R., Biranhu, Y., & Lewi, E. (2020). Ductility and compressibility accommodate high magma flux beneath a silicic continental rift caldera: Insights from Corbetti caldera (Ethiopia). *Geochemistry, Geophysics, Geosystems*, *21*(4), e2020GC008952. https://doi.org/10.1029/2020gc008952

Gualda, G. A., Ghiorso, M. S., Lemons, R. V., & Carley, T. L. (2012). Rhyolite-MELTS: A modified calibration of MELTS optimized for silica-rich, fluid-bearing magmatic systems. *Journal of Petrology*, *53*(5), 875–890. https://doi.org/10.1093/petrology/egr080

Gudmundsson, A. (2005). The effects of layering and local stresses in composite volcanoes on dyke emplacement and volcanic hazards. *Comptes Rendus Geoscience*, *337*(13), 1216–1222. https://doi.org/10.1016/j.crte.2005.07.001

Gudmundsson, A. (2008). *Chapter 8 magma-chamber geometry, fluid transport, local stresses and rock behaviour during collapse caldera formation* (Vol. 10), Elsevier. https://doi.org/10.1016/S1871-644X(07)00008-3

Hamling, I. J., Cevuard, S., & Garaebiti, E. (2019). Large-scale drainage of a complex magmatic system: Observations from the 2018 eruption of Ambrym volcano, Vanuatu. *Geophysical Research Letters*, *46*(9), 4609–4617. https://doi.org/10.1029/2019GL082606

Hautmann, S., Gottsmann, J., Sparks, R. S. J., Mattioli, G. S., Sacks, I. S., & Strutt, M. H. (2010). Effect of mechanical heterogeneity in arc crust on volcano deformation with application to Soufrière Hills Volcano, Montserrat, West Indies. *Journal of Geophysical Research*, *115*(B9), 9203. https://doi.org/10.1029/2009jb006909

Head, M., Hickey, J., Gottsmann, J., & Fournier, N. (2019). The influence of viscoelastic crustal rheologies on volcanic ground deformation: Insights from models of pressure and volume change. *Journal of Geophysical Research: Solid Earth*, *124*(8), 8127–8146. https://doi.org/10.1029/2019jb017832

Heap, M. J., Villeneuve, M., Albino, F., Farquharson, J. I., Brothelande, E., Amelung, F., et al. (2020). Towards more realistic values of elastic moduli for volcano modelling. *Journal of Volcanology and Geothermal Research*, *390*, 106684. https://doi.org/10.1016/j.jvolgeores.2019.106684

Hickey, J., Gottsmann, J., & Del Potro, R. (2013). The large-scale surface uplift in the altiplano-Puna region of Bolivia: A parametric study of source characteristics and crustal rheology using finite element analysis. *Geochemistry, Geophysics, Geosystems*, *14*(3), 540–555. https://doi.org/10.1002/ggge.20057

Huber, C., Townsend, M., Degruyter, W., & Bachmann, O. (2019). Optimal depth of subvolcanic magma chamber growth controlled by volatiles and crust rheology. *Nature Geoscience*, *12*(9), 762–768. https://doi.org/10.1038/s41561-019-0415-6

Huppert, H. E., & Woods, A. W. (2002). The role of volatiles in magma chamber dynamics. *Nature*, *420*(6915), 493–495. https://doi.org/10.1038/nature01211

Hurwitz, S., & Anderson, K. (2019). Temporal variations in scrubbing of magmatic gases at the summit of Kīlauea volcano, Hawai'i. *Geophysical Research Letters*, *46*(24), 14469–14476. https://doi.org/10.1029/2019GL085904

Kilbride, B. M. C., Edmonds, M., & Biggs, J. (2016). Observing eruptions of gas-rich compressible magmas from space. *Nature Communications*, *7*(1), 1–8. https://doi.org/10.1038/ncomms13744

Kilbride, B. M. C., Mulina, K., Wadge, G., Johnson, R. W., Itikarai, I., & Edmonds, M. (2019). Multi-year satellite observations of sulfur dioxide gas emissions and Lava extrusion at Bagana volcano, Papua New Guinea. *Frontiers of Earth Science*, *0*, 9. https://doi.org/10.3389/FEART.2019.00009

Konecke, B. A., Fiege, A., Simon, A. C., Linsler, S., & Holtz, F. (2019). An experimental calibration of a sulfur-in-apatite oxybarometer for mafic systems. *Geochimica et Cosmochimica Acta*, *265*, 242–258. https://doi.org/10.1016/J.GCA.2019.08.044

Liggins, P., Jordan, S., Rimmer, P. B., & Shorttle, O. (2021). Growth and evolution of secondary volcanic atmospheres: I. Identifying the geological character of warm rocky planets. arXiv. Retrieved from https://arxiv.org/abs/2111.05161v1

Liggins, P., Shorttle, O., & Rimmer, P. B. (2020). Can volcanism build hydrogen-rich early atmospheres? *Earth and Planetary Science Letters*, *550*, 116546. https://doi.org/10.1016/J.EPSL.2020.116546

Lindoo, A., Larsen, J. F., Cashman, K. V., & Oppenheimer, J. (2017). Crystal controls on permeability development and degassing in basaltic andesite magma. *Geology*, *45*(9), 831–834. https://doi.org/10.1130/G39157.1

15252027, 2022, 7, Downloaded from https://agupubs.onlinelibrary.wiley.com/doi/10.1029/2022GC010387 by Alaska State Library, Wiley Online Library on [23/06/2025]. See the Terms and Conditions (https://onlinelibrary.wiley.com/terms-and-conditions) on Wiley Online Library for rules of use; OA articles are governed by the applicable Creative Commons License

Lowenstern, J. B. (1994). Dissolved volatile concentrations in an ore-forming magma. *Geology*, *22*(10), 893–896. https://doi.org/10.1130/0091-7613(1994)022

Lu, Z., Dzurisin, D., Lu, Z., & Dzurisin, D. (2014). InSAR imaging of Aleutian volcanoes. In *Insar imaging of aleutian volcanoes* (pp. 87–345). https://doi.org/10.1007/978-3-642-00348-6_6

Masterlark, T. (2003). Finite element model predictions of static deformation from dislocation sources in a subduction zone: Sensitivities to homogeneous, isotropic, Poisson-solid, and half-space assumptions. *Journal of Geophysical Research*, *108*(B11), 2540. https://doi.org/10.1029/2002jb002296

Matjuschkin, V., Blundy, J. D., & Brooker, R. A. (2016). The effect of pressure on sulphur speciation in mid-to deep-crustal arc magmas and implications for the formation of porphyry copper deposits. *Contributions to Mineralogy and Petrology*, *171*(7), 1–25. https://doi.org/10.1007/S00410-016-1274-4

Mogi, K. (1958). Relations between the eruptions of various volcanoes and the deformations of the ground surfaces around them. *Bulletin of the Earthquake Research Institute*, *36*, 99–134. https://doi.org/10.1016/j.epsl.2004.04.016

Morales Rivera, A. M., Amelung, F., & Mothes, P. (2016). Volcano deformation survey over the Northern and Central Andes with ALOS InSAR time series. *Geochemistry, Geophysics, Geosystems*, *17*(7), 2869–2883. https://doi.org/10.1002/2016GC006393

Moran, S. C., Kwoun, O., Masterlark, T., & Lu, Z. (2006). On the absence of InSAR-detected volcano deformation spanning the 1995–1996 and 1999 eruptions of Shishaldin Volcano, Alaska. *Journal of Volcanology and Geothermal Research*, *150*(1–3), 119–131. https://doi.org/10.1016/J.JVOLGEORES.2005.07.013

Mullet, B., & Segall, P. (2022). The surface deformation signature of a transcrustal, crystal mush-dominant magma system. *Journal of Geophysical Research: Solid Earth*, *127*, e2022JB024178. https://doi.org/10.1029/2022JB024178

Naismith, A. K., Matthew Watson, I., Escobar-Wolf, R., Chigna, G., Thomas, H., Coppola, D., & Chun, C. (2019). Eruption frequency patterns through time for the current (1999–2018) activity cycle at Volcán de Fuego derived from remote sensing data: Evidence for an accelerating cycle of explosive paroxysms and potential implications of eruptive activity. *Journal of Volcanology and Geothermal Research*, *371*, 206–219. https://doi.org/10.1016/j.jvolgeores.2019.01.001

Nash, W. M., Smythe, D. J., & Wood, B. J. (2019). Compositional and temperature effects on sulfur speciation and solubility in silicate melts. *Earth and Planetary Science Letters*, *507*, 187–198. https://doi.org/10.1016/J.EPSL.2018.12.006

Neal, C. A., Brantley, S. R., Antolik, L., Babb, J. L., Burgess, M., Calles, K., et al. (2019). The 2018 rift eruption and summit collapse of Kīlauea Volcano. *Science*, *363*(January), 367–374. https://doi.org/10.1126/science.aav7046

O'Neill, H. S. (2021). The thermodynamic controls on sulfide saturation in silicate melts with application to ocean floor basalts. *Magma Redox Geochemistry*, 177–213. https://doi.org/10.1002/9781119473206.CH10

Ohmoto, H., & Kerrick, D. M. (1977). Devolatilization equilibria in graphitic systems. *American Journal of Science*, *277*(8), 1013–1044. https://doi.org/10.2475/ajs.277.8.1013

Okada, Y. (1985). Surface deformation due to shear and tensile faults in a half-space. *Bulletin of the Seismological Society of America*, *75*(4), 1135–1154. https://doi.org/10.1785/bssa0750041135

Papale, P. (1999). Modeling of the solubility of a two-component H2O + CO2 fluid in silicate liquids. *American Mineralogist*, *84*(4), 477–492. https://doi.org/10.2138/am-1999-0402

Papale, P., Moretti, R., & Barbato, D. (2006). The compositional dependence of the saturation surface of H 2O + CO 2 fluids in silicate melts. *Chemical Geology*, *229*(1–3), 78–95. https://doi.org/10.1016/j.chemgeo.2006.01.013

Piochi, M., Bruno, P. P., De Astis, G., Piochi, M., Bruno, P. P., & De Astis, G. (2005). Relative roles of rifting tectonics and magma ascent processes: Inferences from geophysical, structural, volcanological, and geochemical data for the Neapolitan volcanic region (southern Italy). *Geochemistry, Geophysics, Geosystems*, *6*(7). https://doi.org/10.1029/2004GC000885

Plank, T., Kelley, K. A., Zimmer, M. M., Hauri, E. H., & Wallace, P. J. (2013). Why do mafic arc magmas contain ~4wt% water on average? *Earth and Planetary Science Letters*, *364*, 168–179. https://doi.org/10.1016/j.epsl.2012.11.044

Prata, A. J., & Kerkmann, J. (2007). Simultaneous retrieval of volcanic ash and SO_2 using MSG-SEVIRI measurements. *Geophysical Research Letters*, *34*(5). https://doi.org/10.1029/2006GL028691

Pritchard, M. E., Biggs, J., Wauthier, C., Sansosti, E., Arnold, D. W., Delgado, F., et al. (2018). Towards coordinated regional multi-satellite InSAR volcano observations: Results from the Latin America pilot project. *Journal of Applied Volcanology*, *7*(1). https://doi.org/10.1186/s13617-018-0074-0

Rasmussen, D. J., Plank, T. A., Roman, D. C., & Zimmer, M. M. (2022). Magmatic water content controls the pre-eruptive depth of arc magmas. *Science*, *375*(6585), 1169–1172. https://doi.org/10.1126/science.abm5174

Reath, K., Pritchard, M., Biggs, J., Andrews, B., Ebmeier, S. K., Bagnardi, M., & Poland, M. (2020). Using conceptual models to relate multiparameter satellite data to subsurface volcanic processes in Latin America. *Geochemistry, Geophysics, Geosystems*, *21*(1), 1–26. https://doi.org/10.1029/2019GC008494

Reath, K., Pritchard, M., Poland, M., Delgado, F., Carn, S., Coppola, D., et al. (2019). Thermal, deformation, and degassing remote sensing time series (CE 2000–2017) at the 47 most active volcanoes in Latin America: Implications for volcanic systems. *Journal of Geophysical Research: Solid Earth*, *124*(1), 195–218. https://doi.org/10.1029/2018JB016199

Rivalta, E., & Segall, P. (2008). Magma compressibility and the missing source for some dike intrusions. *Geophysical Research Letters*, *35*(4), 1–5. https://doi.org/10.1029/2007GL032521

Robidoux, P., Aiuppa, A., Rotolo, S. G., Rizzo, A. L., Hauri, E. H., & Frezzotti, M. L. (2017). Volatile contents of mafic-to-intermediate magmas at San Cristóbal volcano in Nicaragua. *Lithos*, *272–273*, 147–163. https://doi.org/10.1016/J.LITHOS.2016.12.002

Ruscitto, D. M., Wallace, P. J., Cooper, L. B., & Plank, T. (2012). Global variations in H_2O/Ce: 2. Relationships to arc magma geochemistry and volatile fluxes. *Geochemistry, Geophysics, Geosystems*, *13*(3). https://doi.org/10.1029/2011GC003887

Rust, A. C., & Cashman, K. V. (2011). Permeability controls on expansion and size distributions of pyroclasts. *Journal of Geophysical Research*, *116*(11). https://doi.org/10.1029/2011JB008494

Scaillet, B., & Pichavant, M. (2005). A model of sulphur solubility for hydrous mafic melts: Application to the determination of magmatic fluid compositions of Italian volcanoes. *Annals of Geophysics*.

Sigmarsson, O., Haddadi, B., Carn, S., Moune, S., Gudnason, J., Yang, K., & Clarisse, L. (2013). The sulfur budget of the 2011 Grímsvötn eruption, Iceland. *Geophysical Research Letters*, *40*(23), 6095–6100. https://doi.org/10.1002/2013gl057760

Sigmundsson, F., Pinel, V., Grapenthin, R., Hooper, A., Halldórsson, S. A., Einarsson, P., et al. (2020). Unexpected large eruptions from buoyant magma bodies within viscoelastic crust. *Nature Communications*, *11*(1), 1–11. https://doi.org/10.1038/s41467-020-16054-6

Sparks, R. S., Annen, C., Blundy, J. D., Cashman, K. V., Rust, A. C., & Jackson, M. D. (2019). Formation and dynamics of magma reservoirs. *Philosophical Transactions of the Royal Society A: Mathematical, Physical & Engineering Sciences*, *377*(2139), 20180019. https://doi.org/10.1098/rsta.2018.0019

15252027, 2022, 7, Downloaded from https://agupubs.onlinelibrary.wiley.com/doi/10.1029/2022GC010387 by Alaska State Library, Wiley Online Library on [23/06/2025]. See the Terms and Conditions (https://onlinelibrary.wiley.com/terms-and-conditions) on Wiley Online Library for rules of use; OA articles are governed by the applicable Creative Commons License

Spera, F. J. (2000). Physical properties of magma. Encyclopedia on Volcanoes.
Stephens, K. J., & Wauthier, C. (2018). Satellite geodesy captures offset magma supply associated with Lava lake appearance at Masaya volcano, Nicaragua. *Geophysical Research Letters*, *45*(6), 2669–2678. https://doi.org/10.1002/2017gl076769
Stolper, E., & Walker, D. (1980). Melt density and the average composition of basalt. *Contributions to Mineralogy and Petrology*, *74*(1), 7–12. https://doi.org/10.1007/BF00375484
Telling, J., Flower, V. J., & Carn, S. A. (2015). A multi-sensor satellite assessment of SO_2 emissions from the 2012–13 eruption of Plosky Tolbachik volcano, Kamchatka. *Journal of Volcanology and Geothermal Research*, *307*, 98–106. https://doi.org/10.1016/J.JVOLGEORES.2015.07.010
Theys, N., Hedelt, P., De Smedt, I., Lerot, C., Yu, H., Vlietinck, J., et al. (2019). Global monitoring of volcanic SO_2 degassing with unprecedented resolution from TROPOMI onboard Sentinel-5 Precursor. *Scientific Reports*, *9*(1), 1–10. https://doi.org/10.1038/s41598-019-39279-y
Voight, B., Widiwijayanti, C., Mattioli, G., Elsworth, D., Hidayat, D., & Strutt, M. (2010). Magma-sponge hypothesis and stratovolcanoes: Case for a compressible reservoir and quasi-steady deep influx at Soufrière Hills Volcano, Montserrat. *Geophysical Research Letters*, *37*(19), https://doi.org/10.1029/2009gl041732
Wallace, P. J. (2001). Volcanic SO_2 emissions and the abundance and distribution of exsolved gas in magma bodies. *Journal of Volcanology and Geothermal Research*, *108*(1–4), 85–106. https://doi.org/10.1016/S0377-0273(00)00279-1
Wallace, P. J. (2003). From mantle to atmosphere: Magma degassing, explosive eruptions, and volcanic volatile budgets. *Developments in Volcanology*, *5*(C), 105–127. https://doi.org/10.1016/S1871-644X(03)80026-8
Wallace, P. J. (2005). Volatiles in subduction zone magmas: Concentrations and fluxes based on melt inclusion and volcanic gas data. *Journal of Volcanology and Geothermal Research*, *140*(1–3), 217–240. https://doi.org/10.1016/j.jvolgeores.2004.07.023
Wieser, P. E., Jenner, F., Edmonds, M., Maclennan, J., & Kunz, B. E. (2020). Chalcophile elements track the fate of sulfur at Kīlauea Volcano, Hawai'i. *Geochimica et Cosmochimica Acta*, *282*, 245–275. https://doi.org/10.1016/J.GCA.2020.05.018
Wong, Y., & Segall, P. (2020). Joint inversions of ground deformation, extrusion flux, and gas emissions using Physics-based models for the mount st. Helens 2004–2008 eruption. *Geochemistry, Geophysics, Geosystems*, *21*(12), 1–24. https://doi.org/10.1029/2020GC009343
Wong, Y., Segall, P., Bradley, A., & Anderson, K. (2017). Constraining the magmatic system at mount st. Helens (2004–2008) using Bayesian inversion with Physics-based models including gas escape and crystallization. *Journal of Geophysical Research: Solid Earth*, *122*(10), 7789–7812. https://doi.org/10.1002/2017JB014343
Woods, A. W., & Huppert, H. E. (2003). On magma chamber evolution during slow effusive eruptions. *Journal of Geophysical Research*, *108*(B8), 1–16. https://doi.org/10.1029/2002jb002019
Wu, Z., Wang, X., Liu, J., & Chen, X. (2020). Mineral fibres: Basalt. *Handbook of Natural Fibres*: 2nd ed., *1*, 433–502. https://doi.org/10.1016/B978-0-12-818398-4.00015-3
Yang, X.-M., Davis, P. M., & Dieterich, J. H. (1988). Deformation from inflation of a dipping finite prolate spheroid in an elastic half-space as a model for volcanic stressing. *Journal of Geophysical Research*, *93*(B5), 4249–4257. https://doi.org/10.1029/JB093iB05p04249
Yip, S. T. H., Biggs, J., & Albino, F. (2019). Reevaluating volcanic deformation using atmospheric corrections: Implications for the magmatic system of agung volcano, Indonesia. *Geophysical Research Letters*, *46*(23), 13704–13711. https://doi.org/10.1029/2019GL085233
Zhan, Y., & Gregg, P. M. (2019). How accurately can we model magma reservoir failure with uncertainties in host rock rheology? *Journal of Geophysical Research: Solid Earth*, *124*(8), 8030–8042. https://doi.org/10.1029/2019JB018178
Zhan, Y., Gregg, P. M., Le Mével, H., Miller, C. A., & Cardona, C. (2019). Integrating Reservoir Dynamics, Crustal Stress, and Geophysical Observations of the Laguna del Maule Magmatic System by FEM Models and Data Assimilation. *Journal of Geophysical Research: Solid Earth*, *124*(12), 13547–13562. https://doi.org/10.1029/2019jb018681
Zhang, Y., & Stolper, E. M. (1991). Water diffusion in a basaltic melt. *Nature*, *351*(6324), 306–309.
Zimmer, M. M., Plank, T., Hauri, E. H., Yogodzinski, G. M., Stelling, P., Larsen, J., et al. (2010). The role of water in generating the calc-alkaline trend: New volatile data for Aleutian magmas and a new tholeiitic index. *Journal of Petrology*, *51*(12), 2411–2444. https://doi.org/10.1093/petrology/egq062

References From the Supporting Information

Bachèlery, P., Morin, J., Villeneuve, N., Soulé, H., Nassor, H., & Ali, A. R. (2016). Structure and Eruptive History of Karthala Volcano. *Active Volcanoes of the World*, 345–366. https://doi.org/10.1007/978-3-642-31395-0_22
Bagnardi, M., Amelung, F., & Poland, M. P. (2013). A new model for the growth of basaltic shields based on deformation of Fernandina volcano, Galápagos Islands. *Earth and Planetary Science Letters*, *377-378*, 358–366. https://doi.org/10.1016/j.epsl.2013.07.016
Bani, P., Oppenheimer, C., Allard, P., Shinohara, H., Tsanev, V., Carn, S., et al. (2012). First estimate of volcanic SO_2 budget for Vanuatu island arc. *Journal of Volcanology and Geothermal Research*, *211-212*, 36–46. https://doi.org/10.1016/J.JVOLGEORES.2011.10.005
Bani, P., Oppenheimer, C., Varekamp, J. C., Quiniou, T., Lardy, M., & Carn, S. (2009). Remarkable geochemical changes and degassing at Voui crater lake, Ambae volcano, Vanuatu. *Journal of Volcanology and Geothermal Research*, *188*(4), 347–357. https://doi.org/10.1016/j.jvolgeores.2009.09.018
Bernard, B., Stock, M. J., Coppola, D., Hidalgo, S., Bagnardi, M., Gibson, S., et al. (2019). Chronology and phenomenology of the 1982 and 2015 Wolf volcano eruptions, Galápagos Archipelago. *Journal of Volcanology and Geothermal Research*, *374*. https://doi.org/10.1016/j.jvolgeores.2019.02.013
Bertin, D., Amigo, A., & Bertin, L. (2015). Erupción del volcán Villarrica 2015: Productos emitidos y volumen involucrado. In *Proceedings of the xiv congreso geológico chileno* (pp. 4–8). Retrieved from https://www.researchgate.net/publication/301233640
Biggs, J., Rust, A., & Owens, C. (2014). Deformation at Lava Lake Volcanoes: Lessons from Karthala—NASA/ADS. In *Agu fall meeting abstracts* (pp. V41B–4807). Retrieved from https://ui.adsabs.harvard.edu/abs/2014AGUFM.V41B4807B/abstract
Cameron, C. E., Prejean, S. G., Coombs, M. L., Wallace, K. L., Power, J. A., & Roman, D. C. (2018). Alaska Volcano Observatory Alert and Forecasting Timeliness: 1989–2017. *Frontiers in Earth Science*, *0*, 86. https://doi.org/10.3389/FEART.2018.00086
Chadwick, W. W., Jónsson, S., Geist, D. J., Poland, M., Johnson, D. J., Batt, S., et al. (2011). The May 2005 eruption of Fernandina volcano, Galápagos: The first circumferential dike intrusion observed by GPS and InSAR. *Bulletin of Volcanology*, *73*(6), 679–697. https://doi.org/10.1007/s00445-010-0433-0
Chandni, C. K., & Kumar, S. (2020). DInSAR based analysis of January 2020 eruption of fernandina Volcano, Galapagos. In *2020 IEEE india geoscience and remote sensing symposium, INGARSS 2020—Proceedings*, (pp. 250–253). Institute of Electrical and Electronics Engineers Inc. https://doi.org/10.1109/InGARSS48198.2020.9358954
Dalton, M. P., Waite, G. P., Watson, I. M., & Nadeau, P. A. (2010). Multiparameter quantification of gas release during weak Strombolian eruptions at Pacaya Volcano, Guatemala. *Geophysical Research Letters*, *37*(9), 9303. https://doi.org/10.1029/2010GL042617

15252027, 2022, 7, Downloaded from https://agupubs.onlinelibrary.wiley.com/doi/10.1029/2022GC010387 by Alaska State Library, Wiley Online Library on [23/06/2025]. See the Terms and Conditions (https://onlinelibrary.wiley.com/terms-and-conditions) on Wiley Online Library for rules of use; OA articles are governed by the applicable Creative Commons License

de Leeuw, J., Schmidt, A., Witham, C. S., Theys, N., Taylor, I. A., Grainger, R. G., et al. (2021). The 2019 Raikoke volcanic eruption—Part 1: Dispersion model simulations and satellite retrievals of volcanic sulfur dioxide. *Atmospheric Chemistry and Physics*, *21*(14), 10851–10879. https://doi.org/10.5194/ACP-21-10851-2021

de Moor, J. M., Kern, C., Avard, G., Muller, C., Aiuppa, A., Saballos, A., et al. (2017). A new sulfur and carbon degassing inventory for the southern central American volcanic arc: The importance of accurate time-series data sets and possible tectonic processes responsible for temporal variations in arc-scale volatile emissions. *Geochemistry, Geophysics, Geosystems*, *18*(12), 4437–4468. https://doi.org/10.1002/2017GC007141

Delgado, F., Pritchard, M., Lohman, R., & Naranjo, J. A. (2014). The 2011 Hudson volcano eruption (Southern Andes, Chile): Pre-eruptive inflation and hotspots observed with InSAR and thermal imagery. *Bulletin of Volcanology*, *76*(5), 1–19. https://doi.org/10.1007/S00445-014-0815-9

Derrien, A., Peltier, A., Villeneuve, N., & Staudacher, T. (2020). The 2007 caldera collapse at Piton de la Fournaise: New insights from multi-temporal structure-from-motion. *Volcanica*, *3*(1), 55–65. https://doi.org/10.30909/VOL.03.01.5565

Di Muro, A., Métrich, N., Vergani, D., Rosi, M., Armienti, P., Fougeroux, T., et al. (2014). The Shallow Plumbing System of Piton de la Fournaise Volcano (La Réunion Island, Indian Ocean) Revealed by the Major 2007 Caldera-Forming Eruption. *Journal of Petrology*, *55*(7), 1287–1315. Retrieved from https://academic.oup.com/petrology/article/55/7/1287/1515421%20doi:%2010.1093/PETROLOGY/EGU025

Dirscherl, M., & Rossi, C. (2018). Geomorphometric analysis of the 2014–2015 Bárdarbunga volcanic eruption, Iceland. *Remote Sensing of Environment*, *204*, 244–259. https://doi.org/10.1016/j.rse.2017.10.027

Dvigalo, V. N., Svirid, I. Y., & Shevchenko, A. V. (2014). The first quantitative estimates of parameters for the Tolbachik Fissure Eruption of 2012–2013 from aerophotogrammetric observations. *Journal of Volcanology and Seismology*, *8*(5), 261–268. https://doi.org/10.1134/S0742046314050029

Dzurisin, D., Lu, Z., Poland, M. P., & Wicks, C. W. J. (2019). Space-Based Imaging Radar Studies of U.S. Volcanoes. *Frontiers in Earth Science*, *0*, 249. https://doi.org/10.3389/FEART.2018.00249

Fee, D., Steffke, A., & Garces, M. (2010). Characterization of the 2008 Kasatochi and Okmok eruptions using remote infrasound arrays. *Journal of Geophysical Research: Atmospheres*, *115*(D2), 0–10. https://doi.org/10.1029/2009JD013621

Flower, V. J., & Kahn, R. A. (2020). Interpreting the volcanological processes of Kamchatka, based on multi-sensor satellite observations. *Remote Sensing of Environment*, *237*, 111585. https://doi.org/10.1016/J.RSE.2019.111585

Fournier, T. J., Pritchard, M. E., & Riddick, S. N. (2010). Duration, magnitude, and frequency of subaerial volcano deformation events: New results from Latin America using InSAR and a global synthesis. *Geochemistry, Geophysics, Geosystems*, *11*(1). https://doi.org/10.1029/2009GC002558

Galetto, F., Hooper, A., Bagnardi, M., & Acocella, V. (2020). The 2008 Eruptive Unrest at Cerro Azul Volcano (Galápagos) Revealed by InSAR Data and a Novel Method for Geodetic Modelling. *Journal of Geophysical Research: Solid Earth*, *125*(2), e2019JB018521. https://doi.org/10.1029/2019JB018521

Geist, D. J., Harpp, K. S., Naumann, T. R., Poland, M., Chadwick, W. W., Hall, M., & Rader, E. (2008). The 2005 eruption of Sierra Negra volcano, Galápagos, Ecuador. *Bulletin of Volcanology*, *70*(6), 655–673. https://doi.org/10.1007/s00445-007-0160-3

Gíslason, S. R., Stefánsdóttir, G., Pfeffer, M. A., Barsotti, S., Jóhannsson, T., Galeczka, I., et al. (2015). Environmental pressure from the 2014-15 eruption of Bárdarbunga volcano, Iceland. *Geochemical Perspectives Letters*, *1*, 84–93. https://doi.org/10.7185/geochemlet.1509

Gudmundsson, M. T., Höskuldsson, A., Larsen, G., Thordarson, T., Oladottir, B. A., Oddsson, B., et al. (2012). The May 2011 eruption of Grímsvötn. *Egu general assembly conference abstracts*, *14*, 12119. Retrieved from https://ui.adsabs.harvard.edu/abs/2012EGUGA..1412119G/abstract

Gurioli, L., DI Muro, A., Vlastélic, I., Moune, S., Thivet, S., Valer, M., et al. (2018). Integrating field, textural, and geochemical monitoring to track eruption triggers and dynamics: A case study from Piton de la Fournaise. *Solid Earth*, *9*(2), 431–455. https://doi.org/10.5194/SE-9-431-2018

Harris, A. J., Villeneuve, N., Di Muro, A., Ferrazzini, V., Peltier, A., Coppola, D., et al. (2017). Effusive crises at Piton de la Fournaise 2014–2015: A review of a multi-national response model. *Springer*, *6*(1). https://doi.org/10.1186/s13617-017-0062-9

Henderson, S. T., Pritchard, M. E., Cooper, J. R., & Aoki, Y. (2019). Remotely sensed deformation and thermal anomalies at Mount Pagan, Mariana Islands. *Frontiers in Earth Science*, *0*, 238. https://doi.org/10.3389/FEART.2019.00238

Hreinsdóttir, S., Sigmundsson, F., Roberts, M. J., Björnsson, H., Grapenthin, R., Arason, P., et al. (2014). Volcanic plume height correlated with magma-pressure change at Grímsvötn Volcano, Iceland. *Nature Geoscience*, *7*(3), 214–218. https://doi.org/10.1038/ngeo2044

Johnson, M. S., Schwandner, F. M., Potter, C. S., Nguyen, H. M., Bell, E., Nelson, R. R., et al. (2020). Carbon Dioxide Emissions During the 2018 Kilauea Volcano Eruption Estimated Using OCO_2 Satellite Retrievals. *Geophysical Research Letters*, *47*(24), e2020GL090507. 10.1029/2020GL090507

Kern, C., Lerner, A. H., Elias, T., Nadeau, P. A., Holland, L., Kelly, P. J., et al. (2020). Quantifying gas emissions associated with the 2018 rift eruption of Kīlauea Volcano using ground-based DOAS measurements. *Bulletin of Volcanology 2020*, *82*(7), 1–24. https://doi.org/10.1007/S00445-020-01390-8

Larsen, J., Neal, C., Webley, P., Freymueller, J., Haney, M., McNutt, S., et al. (2009). Eruption of Alaska Volcano Breaks Historic Pattern. *Eos, Transactions American Geophysical Union*, *90*(20), 173. https://doi.org/10.1029/2009eo200001

Liu, E. J., Wood, K., Aiuppa, A., Giudice, G., Bitetto, M., Fischer, T. P., et al. (2021). Volcanic activity and gas emissions along the South Sandwich Arc. *Bulletin of Volcanology*, *83*(1), 1–23. https://doi.org/10.1007/s00445-020-01415-2

Lu, Z., & Dzurisin, D. (2010). Ground surface deformation patterns, magma supply, and magma storage at Okmok volcano, Alaska, from InSAR analysis: 2. Coeruptive deflation, July–August 2008. *Journal of Geophysical Research: Solid Earth*, *115*(B5). https://doi.org/10.1029/2009JB006970

Lundgren, P., Kiryukhin, A., Milillo, P., & Samsonov, S. (2015). Dike model for the 2012–2013 Tolbachik eruption constrained by satellite radar interferometry observations. *Journal of Volcanology and Geothermal Research*, *307*, 79–88. https://doi.org/10.1016/J.JVOLGEORES.2015.05.011

Lundgren, P. R., Bagnardi, M., & Dietterich, H. (2019). Topographic Changes During the 2018 Kīlauea Eruption From Single-Pass Airborne InSAR. *Geophysical Research Letters*, *46*(16), 9554–9562. https://doi.org/10.1029/2019GL083501

McKee, K., Smith, C. M., Reath, K., Snee, E., Maher, S., Matoza, R. S., et al. (2021). Evaluating the state-of-the-art in remote volcanic eruption characterization Part I: Raikoke volcano, Kuril Islands. *Journal of Volcanology and Geothermal Research*, *419*, 107354. https://doi.org/10.1016/J.JVOLGEORES.2021.107354

Morgan, H. A., Harris, A. J., & Gurioli, L. (2013). Lava discharge rate estimates from thermal infrared satellite data for Pacaya Volcano during 2004–2010. *Journal of Volcanology and Geothermal Research*, *264*, 1–11. https://doi.org/10.1016/J.JVOLGEORES.2013.07.008

Morin, J., Lavigne, F., Bachelery, P., Finizola, A., & Villeneuve, N. (2009). Morin et al-Responses to Hazards, Karthala (Comoros) Part I institutional and social responses to hazards related to Karthala Volcano, Comoros. *The International Journal of Research into Island Cultures*, *3*, 33–53.

15252027, 2022, 7, Downloaded from https://agupubs.onlinelibrary.wiley.com/doi/10.1029/2022GC010387 by Alaska State Library, Wiley Online Library on [23/06/2025]. See the Terms and Conditions (https://onlinelibrary.wiley.com/terms-and-conditions) on Wiley Online Library for rules of use; OA articles are governed by the applicable Creative Commons License

Moussallam, Y., Rose-Koga, E. F., Koga, K. T., Médard, E., Bani, P., Devidal, J. L., & Tari, D. (2019). Fast ascent rate during the 2017–2018 Plinian eruption of Ambae (Aoba) volcano: A petrological investigation. *Contributions to Mineralogy and Petrology*, *174*(11), 1–24. https://doi.org/10.1007/S00410-019-1625-Z/FIGURES/13

Németh, K., & Cronin, S. J. (2008). Volcanic craters, pit craters and high-level magma-feeding systems of a Mafic Island-arc volcano: Ambrym, Vanuatu, South Pacific. *Geological Society, London, Special Publications*, *302*(1), 87–102. https://doi.org/10.1144/SP302.6

Pardini, F., Queißer, M., Naismith, A., Watson, I. M., Clarisse, L., & Burton, M. R. (2019). Initial constraints on triggering mechanisms of the eruption of Fuego volcano (Guatemala) from 3 June 2018 using IASI satellite data. *Journal of Volcanology and Geothermal Research*, *376*, 54–61. https://doi.org/10.1016/J.JVOLGEORES.2019.03.014

Peltier, A., Beauducel, F., Villeneuve, N., Ferrazzini, V., Di Muro, A., Aiuppa, A., et al. (2016). Deep fluid transfer evidenced by surface deformation during the 2014–2015 unrest at Piton de la Fournaise volcano. *Journal of Volcanology and Geothermal Research*, *321*, 140–148. https://doi.org/10.1016/J.JVOLGEORES.2016.04.031

Peltier, A., Villeneuve, N., Ferrazzini, V., Testud, S., Hassen Ali, T., Boissier, P., & Catherine, P. (2018). Changes in the long-term geophysical eruptive precursors at Piton de la Fournaise: Implications for the response management. *Frontiers in Earth Science*, *6*, 104. https://doi.org/10.3389/FEART.2018.00104/BIBTEX

Prata, A. J., Gangale, G., Clarisse, L., & Karagulian, F. (2010). Ash and sulfur dioxide in the 2008 eruptions of Okmok and Kasatochi: Insights from high spectral resolution satellite measurements. *Journal of Geophysical Research*, *115*(22), D00L18. http://doi.wiley.com/10.1029/2009JD013556

Richter, N., & Froger, J. L. (2020). The role of Interferometric Synthetic Aperture Radar in Detecting, Mapping, Monitoring, and Modelling the Volcanic Activity of Piton de la Fournaise, La Réunion: A Review. *Remote Sensing 2020*, *12*(6), 1019. https://doi.org/10.3390/RS12061019

Stock, M. J., Bagnardi, M., Neave, D. A., Maclennan, J., Bernard, B., Buisman, I., et al. (2018). Integrated petrological and geophysical constraints on magma system architecture in the western Galápagos Archipelago: Insights from wolf volcano. *Geochemistry, Geophysics, Geosystems*, *19*(12), 4722–4743. https://doi.org/10.1029/2018GC007936

Thivet, S., Gurioli, L., Muro, A. D., Derrien, A., Ferrazzini, V., Gouhier, M., et al. (2020). Evidences of plug pressurization enhancing magma fragmentation during the September 2016 basaltic eruption at Piton de la Fournaise (La Réunion Island, France). *Geochemistry, Geophysics, Geosystems*, *21*(2), e2019GC008611. https://doi.org/10.1029/2019GC008611

Thordarson, T., & Hartley, M. (2015). Atmospheric sulfur loading by the ongoing Nornahraun eruption, North Iceland. *Geophysical Research Abstracts*, *17*, Retrieved from http://www.ust.is/einstaklingar/loftgaedi/maelingar/

Tulet, P., & Villeneuve, N. (2011). Large scale modeling of the transport, chemical transformation and mass budget of the sulfur emitted during the April 2007 eruption of Piton de la Fournaise. *Atmospheric Chemistry and Physics*, *11*(9), 4533–4546. https://doi.org/10.5194/ACP-11-4533-2011

Valade, S., Ley, A., Massimetti, F., D'Hondt, O., Laiolo, M., Coppola, D., et al. (2019). Towards Global Volcano Monitoring Using Multisensor Sentinel Missions and Artificial Intelligence: The MOUNTS Monitoring System. *Remote Sensing 2019*, *11*(13), 1528. https://doi.org/10.3390/RS11131528

Vasconez, F., Ramón, P., Hernandez, S., Hidalgo, S., Bernard, B., Ruiz, M., et al. (2018). The different characteristics of the recent eruptions of Fernandina and Sierra Negra volcanoes (Galápagos, Ecuador). *Volcanica*, *1*(2), 127–133. https://doi.org/10.30909/vol.01.02.127133

Waythomas, C. F., Scott, W. E., Prejean, S. G., Schneider, D. J., Izbekov, P., & Nye, C. J. (2010). The 7–8 August 2008 eruption of Kasatochi Volcano, central Aleutian Islands, Alaska. *Journal of Geophysical Research: Solid Earth*, *115*(B12). https://doi.org/10.1029/2010JB007437

Wnuk, K., & Wauthier, C. (2017). Surface deformation induced by magmatic processes at Pacaya Volcano, Guatemala revealed by InSAR. *Journal of Volcanology and Geothermal Research*, *344*, 197–211. https://doi.org/10.1016/J.JVOLGEORES.2017.06.024

Xu, W., Jónsson, S., Ruch, J., & Aoki, Y. (2016). The 2015 Wolf volcano (Galápagos) eruption studied using Sentinel-1 and ALOS-2 data. *Geophysical Research Letters*, *43*(18). https://doi.org/10.1002/2016GL069820

15252027, 2022, 7, Downloaded from https://agupubs.onlinelibrary.wiley.com/doi/10.1029/2022GC010387 by Alaska State Library, Wiley Online Library on [23/06/2025]. See the Terms and Conditions (https://onlinelibrary.wiley.com/terms-and-conditions) on Wiley Online Library for rules of use; OA articles are governed by the applicable Creative Commons License